EarthArXiv Coversheet

Local Prediction of Temperate Forest Structure in Eastern North America Using LiDAR, Radar, and Optical Data

Authors

Chenyang Wei[1], Colin Sweeney[1], Trevor Roberts[2], Hikaru Keebler[1], Daniel Fink[3], Benjamin Zuckerberg[2], Marta A Jarzyna[1,4], Kaiguang Zhao[5]

Affiliations

[1] Department of Evolution, Ecology and Organismal Biology, The Ohio State University, Columbus, OH, United States of America

[2] Department of Forest and Wildlife Ecology, University of Wisconsin-Madison, Madison, WI, United States of America

[3] Lab of Ornithology, Cornell University, Ithaca, NY, United States of America

[4] Translational Data Analytics Institute, The Ohio State University, Columbus, OH, United States of America

[5] School of Environment and Natural Resources, The Ohio State University, Columbus, United States of America

Corresponding author

Chenyang Wei (ChenyangWei.CWei@gmail.com)

Peer status statement: This document is a non-peer-reviewed preprint submitted to EarthArXiv. The manuscript has been submitted to Environmental Research Letters for peer review (submitted October 30, 2025). If accepted, a postprint update will include the journal citation and DOI.

Keywords

GEDI; LiDAR; vegetation structure; temperate forest; eastern North America; local modeling; machine learning

Title

Local Prediction of Temperate Forest Structure in Eastern North America Using LiDAR, Radar, and Optical Data

Keywords

GEDI, LiDAR, vegetation structure, temperate forest, eastern North America, local modeling, machine learning

Abstract

Forest structure underpins the emergence of ecological patterns and processes yet remains costly and labor-intensive to measure at broad scales. NASA's Global Ecosystem Dynamics Investigation (GEDI) mission provides three-dimensional Light Detection and Ranging (LiDAR) measurements at discrete footprints, leaving spatial gaps that complicate wall-to-wall mapping. Few studies have produced high-resolution, broad-extent predictions of multiple GEDI-derived metrics while explicitly accounting for spatial nonstationarity in predictor–response relationships. We addressed this gap with a local modeling framework that predicted 11 GEDI-based structural metrics at 30-m resolution across temperate broadleaf and mixed forests of eastern North America (1.17 million km^2) for 2019–2022. Using Google Earth Engine, we integrated Landsat and Sentinel-2 multispectral imagery, Sentinel-1 synthetic aperture radar, and auxiliary variables (topography, land cover, leaf traits, and soil properties) to derive 93 environmental covariates. We partitioned the study area into 1,693 overlapping tiles, trained tile-specific random forest (RF) models with 80% of GEDI observations, and aggregated overlaps using weights based on model performance and pixel location. Across all metrics, local model predictions correlated strongly with GEDI measurements (Pearson's $r > 0.65$). On the 20% held-out test set, median R^2 of local models exceeded 0.4 for seven metrics, with canopy height and canopy cover both reaching 0.63. Sentinel-2, topography, and Landsat ranked among the most important predictor groups in at least 69.6% of local models for each metric. Across 30 randomly sampled tiles, local models outperformed a single global RF model in 56.7% of cases, with the largest gains where the global model performed worst. Our results show that integrating spaceborne LiDAR with multisource environmental covariates in a local modeling framework delivers robust predictions of forest structure and offers a transferable approach across broad geographic regions.

1. Introduction

Forest structure, the volumetric capacity and the spatial arrangement of vegetative components of different identities (LaRue *et al* 2023), affects the composition, dynamics, and functioning of forest ecosystems (Nadkarni *et al* 2008). It shapes the availability of physical space and resources, which constrains the number of individuals a community can harbor (Camacho *et al* 2025) and underpins the diversity of ecological niches that support coexisting life forms (MacArthur and MacArthur 1961, Stein *et al* 2014). Forest structural properties also mediate plant responses to climate warming by influencing canopy light-use efficiency, light absorption, productivity, and understory microclimate (Gough *et al* 2019, Atkins *et al* 2018, Ray *et al* 2023, Zellweger *et al* 2020). A deeper understanding of forest structure is thus essential for advancing both wildlife habitat assessments and carbon stock estimation in terrestrial ecosystems. Despite this importance, field-based measurement of fine-scale forest structure across broad extents requires substantial labor, time, and cost, which limits most studies to local or landscape scales (Bakx *et al* 2019).

Light Detection and Ranging (LiDAR), an active remote sensing technology, offers a cost-effective, efficient, and scalable means of mapping forest structure across large spatial extents (Hakkenberg and Goetz 2021, Bakx *et al* 2019, Tamiminia *et al* 2024). As a pioneering space-borne LiDAR mission, NASA's Global Ecosystem Dynamics Investigation (GEDI) was designed to consistently measure ecosystem structure at near-global scales (Dubayah *et al* 2020, 2022). Using full-waveform LiDAR, GEDI records complete vertical vegetation profiles at 25-m footprints, enabling prediction of key structure-related ecosystem properties, such as canopy height (Potapov *et al* 2021, Lang *et al* 2023), canopy cover (Schlickmann *et al* 2025, Seyrek *et al* 2025), plant area index (PAI, Ziegler *et al* 2023, Marselis *et al* 2022), vegetation structural heterogeneity (de Conto *et al* 2024, Rishmawi *et al* 2022), and aboveground biomass density (Dubayah *et al* 2022, Duncanson *et al* 2022).

Despite broad use for predicting structure-relevant ecosystem properties, GEDI poses several challenges, including sparse and uneven spatial coverage and large data volume (Burns *et al* 2024, 2025, Potapov *et al* 2021). To produce wall-to-wall maps of forest structure, researchers commonly adopt three approaches: 1) aggregate footprint-level measurements into coarser spatial units using summary statistics (Killion *et al* 2023, Xu *et al* 2024, Burns *et al* 2024, Xu *et al* 2025, Marselis *et al* 2022, Liu *et al* 2025); 2) interpolate discrete GEDI observations to generate continuous rasters (Mohammadpour *et al* 2025, Ren *et al* 2023, Burns *et al* 2020); and 3) predict GEDI-derived structural metrics with data-fusion models that leverage continuous-coverage covariates, such as multispectral imagery, Synthetic Aperture Radar (SAR), and digital elevation models (DEMs) (Tamiminia *et al* 2024, Schlickmann *et al* 2025, Favrichon *et al* 2025, Ngo *et al* 2023, Lang *et al* 2023, Vogeler *et al* 2023, Ziegler *et al* 2023, Seyrek *et al* 2025, Kacic *et al* 2023). Aggregation works best where GEDI sampling is dense (Burns *et al* 2024); when sampling thins, analysts often coarsen grid cells to raise within-cell density, which reduces the ability to capture local variability in forest structure (Killion *et al* 2023, Xu *et al* 2025, 2024). Interpolation

accuracy and reliability generally improve as data density increases (Lu and Wong 2008, Loiseau *et al* 2021), yet methods such as inverse distance weighting and Simple or Ordinary Kriging rely on spatial proximity or correlation among GEDI observations and typically ignore environmental covariates that explain ecological drivers of forest structure. Data-fusion models offer stronger performance for large-area interpolation and for filling sparsely sampled grid cells (Burns *et al* 2020), but the volume of GEDI and auxiliary data and the associated computation force trade-offs among geographic extent, spatial resolution, and the number of structural metrics. Many studies therefore prioritize one or two of these aspects at the expense of the others: some map large extents at coarse resolution, for example > 100 m (Rishmawi *et al* 2021, Sothe *et al* 2022, Rishmawi *et al* 2022), while others favor fine resolution but focus on regional scales (e.g., < 0.5 million km^2) with limited latitudinal or elevational gradients (Tamiminia *et al* 2024, Schlickmann *et al* 2025, Kacic *et al* 2021, Ziegler *et al* 2023, Ngo *et al* 2023, Favrichon *et al* 2025, Seyrek *et al* 2025, Kacic *et al* 2023), or target a single metric, such as canopy height (Potapov *et al* 2021, Ngo *et al* 2023, Favrichon *et al* 2025, Lang *et al* 2023, Sothe *et al* 2022), canopy cover (Schlickmann *et al* 2025, Seyrek *et al* 2025), or PAI (Ziegler *et al* 2023). Few studies address high spatial resolution, broad extent, and multiple metrics simultaneously. Two notable exceptions come from Vogeler et al. (2023) and Burns et al. (2025), which use global data-fusion models to produce maps at relatively high spatial resolutions (30 m and 90 m) for multiple GEDI-derived forest structural metrics across relatively large regions.

Global models estimate a single relationship between predictors and response across an entire region, assuming that the same process operates everywhere (Fink *et al* 2010, Finley 2011). While useful for prediction, global models can overlook nonstationary relationships between forest structure and environmental conditions across heterogeneous landscapes (Potapov *et al* 2021). Local models, on the other hand, restrict training to limited neighborhoods, which enables them to capture local patterns, limit extrapolation, and adapt to spatially varying predictor–response relationships that may improve prediction in heterogeneous systems (Fink *et al* 2010). Local models also reduce data volume, enable parallel processing, and lower computational burden (Kacic *et al* 2021, Potapov *et al* 2021).

In this study, we developed a local data-fusion modeling framework to predict 11 GEDI-based forest structural metrics across 1.17 million km^2 of eastern North America for 2019–2022. We partitioned the region into 1,693 overlapping tiles and derived 93 environmental covariates per tile. We trained tile-specific random forest (RF) models to predict each metric at 30-m resolution and composited overlaps with weights based on local model accuracy and pixel location. We validated predictions with held-out and randomly sampled GEDI observations and compared predictor importance across covariate groups and benchmarked local models against global counterparts. Our approach can be adapted to Google Earth Engine (GEE) to meet data volume and computational requirements (Gorelick *et al* 2017). In doing so, our goal was to advance understanding and prediction of forest structure across heterogeneous landscapes in eastern North America.

2. Methods

2.1. Study Area

We delineated the mid-latitude temperate broadleaf and mixed forests of eastern North America (Dinerstein *et al* 2017), where GEDI observation density was relatively high and vegetation density was relatively low (Burns *et al* 2024). The study area spanned broad latitudinal and elevational gradients from northeastern Alabama, USA, to southeastern Quebec, Canada, and included four Bird Conservation Regions (BCRs) defined by the North American Bird Conservation Initiative (figure 1): (a) Lower Great Lakes/St. Lawrence Plain (BCR ID: 13), (b) Atlantic Northern Forest (BCR ID: 14), (c) Appalachian Mountains (BCR ID: 28), and (d) Piedmont (BCR ID: 29).

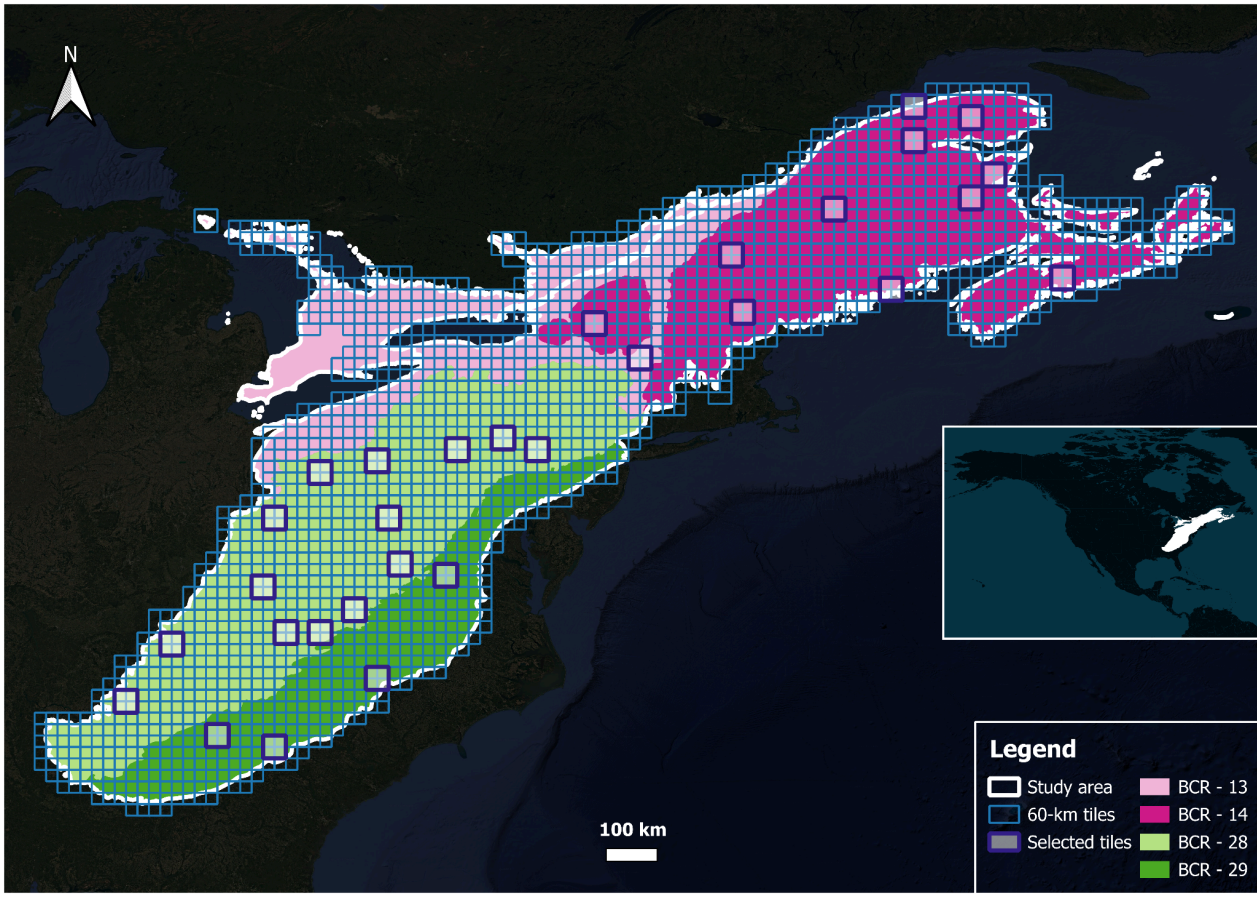

Figure 1. Study area (white-bordered polygon) in eastern North America includes four Bird Conservation Regions (BCRs) as defined by the North American Bird Conservation Initiative: (a) Lower Great Lakes/St. Lawrence Plain (BCR ID: 13), (b) Atlantic Northern Forest (BCR ID: 14), (c) Appalachian Mountains (BCR ID: 28), and (d) Piedmont (BCR ID: 29). The inset shows the study area as the white-filled region. Blue squares show 1,693 modeling units (60-km tiles). White semitransparent squares with thick purple borders mark the tiles for model performance evaluation. We exclude the nonforested western portion of the Lower Great Lakes/St. Lawrence Plain, so 60-km tiles do not cover that area.

2.2. GEDI Data Collection and Preprocessing

We used Version 2 of the GEDI Level 2A (L2A) and Level 2B (L2B) footprint-level canopy height and profile metrics (Beck *et al* 2021, Dubayah *et al* 2020, 2021a, 2021b), which are stored as 25-m resolution raster files in GEE. Version 2 incorporates refined algorithm settings for laser shot selection and significantly reduces geolocation errors in orbital segments (Tang *et al* 2023, Li *et al* 2024a). We collected GEDI observations during the primary growing season (May through September) from 2019 to 2022 (figure 2c). This temporal window was chosen to minimize the influence of phenological variability in mixed and deciduous forests and to reduce the potential effects of snow cover across the study area (Lang *et al* 2023, Favrichon *et al* 2025, Vogeler *et al* 2023). Furthermore, since GEDI LiDAR signals are known to underestimate canopy height during leaf-off periods (Li *et al* 2024b), we restricted our analysis to waveforms acquired under leaf-on conditions by applying the "leaf_off_flag" available in the GEDI data products (Marselis *et al* 2022, Potapov *et al* 2021, Li *et al* 2023, Burns *et al* 2024, Rishmawi *et al* 2022).

(a) Geographic location of the tile example

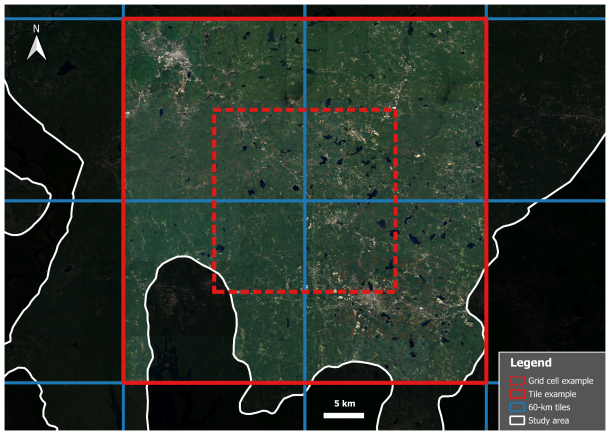

(b) 60-km tile example

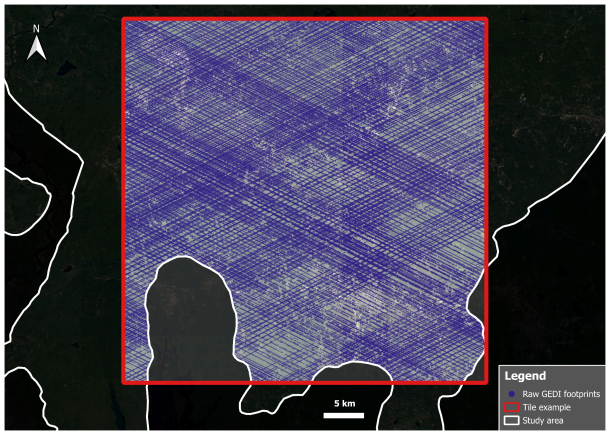

(c) Original GEDI footprints

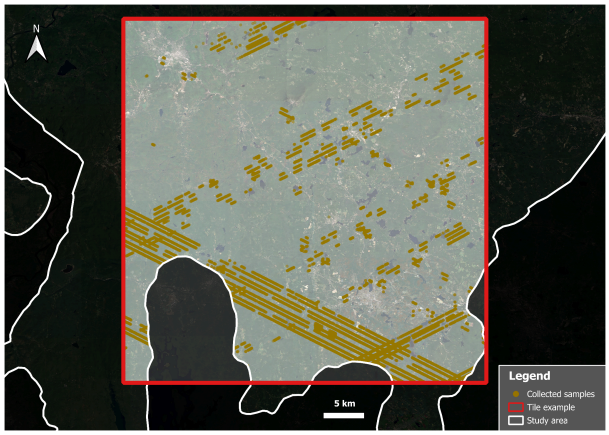

(d) Collected GEDI observations

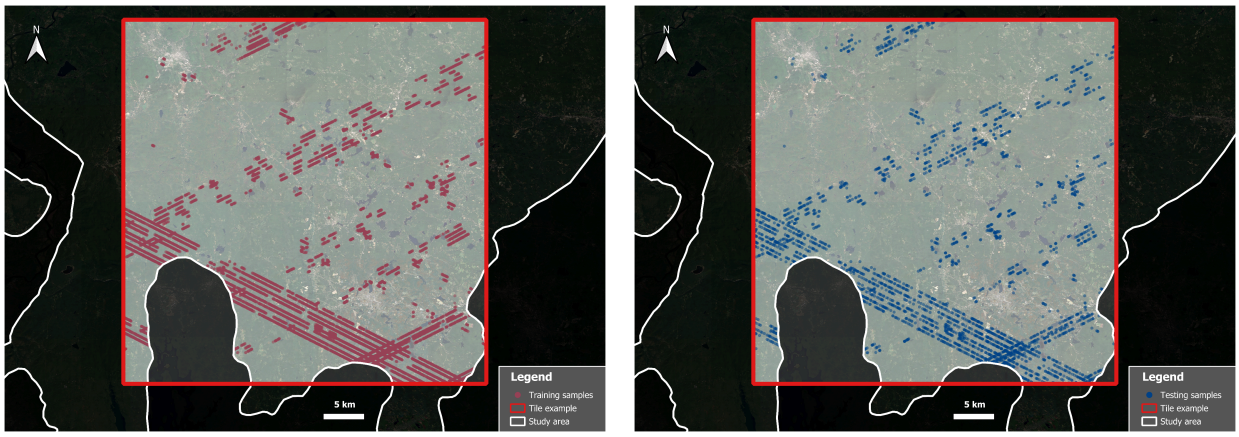

(e) Training observations **(f)** Testing observations

Figure 2. GEDI data preprocessing in one example of the 1,693 modeling units (i.e., 60-km tiles) in this study. **(a)** Geographic location of the tile example (the red square) in the study area (the white polygon). **(b)** 60-km tile example (the red solid square), the corresponding 30-km grid cell (the red dotted square), and the overlapped 60-km tiles (blue squares) on top of the study area (the white polygon). **(c)** Geographic locations of original GEDI footprints (purple dots) within the tile example. **(d)** Collected GEDI observations (yellow dots) after data filtering. **(e)** and **(f)** Subsets of the collected GEDI observations used for model training (red dots) and testing (blue dots), respectively. GEDI footprint sizes shown in each map are slightly exaggerated for visualization purposes.

To ensure the reliability of GEDI-derived forest structural metrics, we applied a series of quality filters to retain only high-quality L2 observations (see Supplementary material, section S1: GEDI data filtering). We selected metrics that captured footprint-level and vertical layering properties (table 1). From GEDI L2A, we used RH98, the relative height at which 98% of waveform energy returned, as the canopy height metric because it showed less noise than RH100 (Li *et al* 2024b, Ngo *et al* 2023). To quantify horizontal extent and vertical density, we extracted total canopy cover fraction and total PAI from GEDI L2B. To represent forest structural heterogeneity, we included foliage height diversity (FHD) from GEDI L2B to summarize vertical foliage distribution.

Table 1. GEDI-derived forest structural metrics in this study. The derivation of each metric is based on the corresponding GEDI Level 2 (L2) variables described by their science dataset names, including rh (relative height metrics at 1% interval, source: L2A dataset), cover (total canopy cover fraction, source: L2B dataset), pai (total plant area index, source: L2B dataset), fhd_normal (foliage height diversity, source: L2B dataset), and pavd_z (plant area volume density profile, source: L2B dataset).

Type	Category	Name	Description	Derivation	Unit
Footprint level	--	Canopy height	Canopy height	$rh98$	m
		Canopy cover	Total canopy cover fraction	$cover$	--
		PAI	Total plant area index	pai	m^2/m^2
		FHD	Foliage height diversity	fhd_normal	--
Vertical layering	Fixed-stratum density	$PAVD_{0–10m}$	Plant area volume density between 0 m and 10 m	$\frac{pavd\_z0 + pavd\_z1}{2}$	m^2/m^3
		$PAVD_{10–20m}$	Plant area volume density between 10 m and 20 m	$\frac{pavd\_z2 + pavd\_z3}{2}$	
		$PAVD_{20–30m}$	Plant area volume density between 20 m and 30 m	$\frac{pavd\_z4 + pavd\_z5}{2}$	
		$PAVD_{30–40m}$	Plant area volume density between 30 m and 40 m	$\frac{pavd\_z6 + pavd\_z7}{2}$	
	Relative height range	$RHD_{25–50\%}$	Relative height difference between 25% and 50%	$rh50 - rh25$	m
		$RHD_{50–75\%}$	Relative height difference between 50% and 75%	$rh75 - rh50$	
		$RHD_{75–98\%}$	Relative height difference between 75% and 98%	$rh98 - rh75$	

In addition to footprint-level metrics, we quantified vertical distribution within each GEDI footprint by computing plant area volume density (PAVD) profiles in 10-m strata from 0 to 40 m (table 1), recognizing that most trees in the study area fall within this height range. We also derived the vertical extent of relative height quartiles for each GEDI footprint, using RH25 through RH98 to represent the cumulative energy distribution of the returned waveform (table 1).

To resolve overlap among GEDI footprints, we computed the median of each forest structural metric for each distinct footprint location across observations over the study period. This approach ensured consistent measurements across footprints and reduced the influence of uneven spatial coverage, variable cloud contamination, seasonal shifts in vegetation phenology, and extreme outlier values. To ultimately predict the GEDI-derived forest structural metrics in eastern North America, we used GEE to derive 93 environmental predictors from seven groups, which represented a wide range of environmental conditions relevant to forest structure (table 2; Supplementary material, section S2: Environmental predictor determination and preprocessing).

Table 2. Environmental predictors used to predict GEDI-derived forest structural metrics in eastern North America. Landsat 8/9, Sentinel-2, and Sentinel-1 predictors use imagery acquired from May to September in 2019–2022, and land cover predictors use annual products for 2019–2022.

Group	Temporal resolution	Class	Spatial resolution	Name	Description and derivation	References
Group 1: Landsat-8/9 (HLSL30) & **Group 2:** Sentinel-2 (S2)	HLSL30: 2–3 days S2: 5 days	Surface reflectance (SR)	HLSL30: 30 m S2: 10 m for Bands 2, 3, 4, 8; 20 m for ***Bands 5, 6, 7, 8A, 11, 12***	Blue	HLSL30: Temporal median SR of Band 2 S2: Temporal median SR of Band 2	HLSL30: (Masek *et al* 2021, Claverie *et al* 2018) S2: (Copernicus n.d.)
				Green	HLSL30: Temporal median SR of Band 3 S2: Temporal median SR of Band 3	
				Red	HLSL30: Temporal median SR of Band 4 S2: Temporal median SR of Band 4	
				Red Edge 1	S2: Temporal median SR of ***Band 5***	
				Red Edge 2	S2: Temporal median SR of ***Band 6***	
				Red Edge 3	S2: Temporal median SR of ***Band 7***	
				Near infrared (NIR)	HLSL30: Temporal median SR of Band 5 S2: Temporal median SR of Band 8	
				Red Edge 4	S2: Temporal median SR of ***Band 8A***	
				Shortwave infrared-1 (SWIR1)	HLSL30: Temporal median SR of Band 6 S2: Temporal median SR of ***Band 11***	
				Shortwave infrared-2 (SWIR2)	HLSL30: Temporal median SR of Band 7 S2: Temporal median SR of ***Band 12***	
		Vegetation index	30 m	Normalized difference vegetation index (NDVI)	$\frac{NIR - Red}{NIR + Red}$	(Rouse *et al* 1974, Tucker 1979)
				Enhanced vegetation index (EVI)	$2.5 \cdot \frac{NIR - Red}{NIR + 6 \cdot Red - 7.5 \cdot Blue + 1}$	(Huete *et al* 2002)
				Near-infrared reflectance of vegetation (NIR_V)	$NDVI \cdot NIR$	(Badgley *et al* 2017)
				Kernel normalized difference vegetation index (kNDVI)	$tanh(NDVI^2)$	(Camps-Valls *et al* 2021)
				Normalized difference water index (NDWI)	$\frac{NIR - SWIR1}{NIR + SWIR1}$	(Gao 1996)
		Environmental index	30 m	Normalized burn ratio (NBR)	$\frac{NIR - SWIR2}{NIR + SWIR2}$	(Key and Benson 2006)
				Bare soil index (BSI)	$\frac{(SWIR1 + Red) - (NIR + Blue)}{(SWIR1 + Red) + (NIR + Blue)}$	(Rikimaru *et al* 2002)
				Build-up index (BU)	$-NDWI - NDVI$	(He *et al* 2010)

			Shadow index (SI)	$\sqrt[3]{\prod_{b \in B}(1 - b)}$ $B = \{Red, Green, Blue\}$	(Rikimaru *et al* 2002)
			Modified normalized difference water index (MNDWI)	$\frac{Green - SWIR1}{Green + SWIR1}$	(Xu 2006)
		Tasseled-cap-transformation index 30 m	Brightness	HLSL30: $0.3690 \cdot Blue + 0.4271 \cdot Green + 0.4689 \cdot Red + 0.5073 \cdot NIR + 0.3824 \cdot SWIR1 + 0.2406 \cdot SWIR2$ S2: $0.3510 \cdot Blue + 0.3813 \cdot Green + 0.3437 \cdot Red + 0.7196 \cdot NIR + 0.2396 \cdot SWIR1 + 0.1949 \cdot SWIR2$	HLSL30: (Zhai *et al* 2022) S2: (Shi and Xu 2019)
			Greenness	HLSL30: $-0.2870 \cdot Blue - 0.2685 \cdot Green - 0.4087 \cdot Red + 0.8145 \cdot NIR + 0.0637 \cdot SWIR1 - 0.1052 \cdot SWIR2$ S2: $-0.3599 \cdot Blue - 0.3533 \cdot Green - 0.4734 \cdot Red + 0.6633 \cdot NIR + 0.0087 \cdot SWIR1 - 0.2856 \cdot SWIR2$	
			Wetness	HLSL30: $0.0382 \cdot Blue + 0.2137 \cdot Green + 0.3536 \cdot Red + 0.2270 \cdot NIR - 0.6108 \cdot SWIR1 - 0.6351 \cdot SWIR2$ S2: $0.2578 \cdot Blue + 0.2305 \cdot Green + 0.0883 \cdot Red + 0.1071 \cdot NIR - 0.7611 \cdot SWIR1 - 0.5308 \cdot SWIR2$	
Group 3: Sentinel-1	6 days	Polarization 10 m	Vertical-horizontal polarization (σ^0_{VH})	Temporal median of the cross-polarized backscattering coefficient of the vertical transmit and horizontal receive polarization	(Copernicus n.d.)
			Vertical-vertical polarization (σ^0_{VV})	Temporal median of the co-polarized backscattering coefficient of the vertical transmit and vertical receive polarization	
		Radar index 10 m	VH/VV polarization ratio	$\frac{\sigma^0_{VH}}{\sigma^0_{VV}}$	(Copernicus n.d., Schlund and Erasmi 2020)
			Radar normalized difference vegetation index (RNDVI)	$\frac{\sigma^0_{VH} - \sigma^0_{VV}}{\sigma^0_{VH} + \sigma^0_{VV}}$	(Mastro *et al* 2023)
			Radar vegetation index (RVI)	$\frac{4 \cdot \sigma^0_{VH}}{\sigma^0_{VV} + \sigma^0_{VH}}$	(Nasirzadehdizaji *et al* 2019)
Group 4: Land cover	Annual	S2-based 10 m	Land cover class	Temporally most common land cover class	(Karra *et al* 2021)
	Annual	Landsat-based 30 m	Land cover class	Temporally most common land cover class	(Zhang *et al* 2024b, Liu *et al* 2023)

Group 5: Topography	--	Digital surface model	30 m	Elevation Slope Aspect	(Takaku *et al* 2016, 2020, Tadono *et al* 2016)
				East-westness index $sin(Slope \cdot \frac{\pi}{180^\circ}) \cdot sin(Aspect \cdot \frac{\pi}{180^\circ})$ North-southness index $sin(Slope \cdot \frac{\pi}{180^\circ}) \cdot cos(Aspect \cdot \frac{\pi}{180^\circ})$	(Sherman *et al* 2008, Wilson *et al* 2015)
		Topographic feature	90 m	Landform classes Continuous Heat-Insolation Load Index (CHILI)	(Theobald *et al* 2015)
			270 m	Topographic diversity Multi-scale Topographic Position Index (mTPI)	(Theobald *et al* 2015)
Group 6: Leaf trait	--	--	1,000 m	Specific leaf area Leaf dry matter content Leaf nitrogen content per dry mass Leaf phosphorus content per dry mass	(Moreno-Martínez *et al* 2018)
Group 7: Soil property	--	For each topsoil layer: 0–5 cm; 5–15 cm; 15–30 cm	250 m	Bulk density of the fine earth fraction Cation exchange capacity of the soil Volumetric fraction of coarse fragments (> 2 mm) Proportion of clay particles (< 0.002 mm) in the fine earth fraction Total nitrogen Soil pH Proportion of sand particles (> 0.05 mm) in the fine earth fraction Proportion of silt particles (≥ 0.002 mm and ≤ 0.05 mm) in the fine earth fraction Soil organic carbon content in the fine earth fraction Organic carbon density	(Poggio *et al* 2021)
		For the full 0–30 cm topsoil layer	250 m	Organic carbon stocks	(Poggio *et al* 2021)

2.3. Local Data-Fusion Modeling

We developed a local data-fusion framework in GEE that integrated GEDI observations with the 93 environmental predictors (table 2) and generated 30-m predictive maps of the 11 forest structural metrics (table 1) across eastern North America. We used the random forest (RF) model (Breiman 2001), a nonparametric machine-learning ensemble technique that effectively handles high data dimensionality and multicollinearity, operates efficiently, and resists overfitting (Belgiu and Drăguţ 2016). Prior studies have demonstrated strong performance of RF models for

GEDI-based prediction of vegetation structural metrics (Vogeler *et al* 2023, Schlickmann *et al* 2025, Seyrek *et al* 2025, Ziegler *et al* 2023, Wei *et al* 2024, Ngo *et al* 2023, Tamiminia *et al* 2024, Kacic *et al* 2023, Burns *et al* 2025). To fit local RF models that related each forest structural metric to the 93 environmental covariates, we resampled each environmental predictor to the 25-m GEDI pixels and retained only observations with no missing values for all the forest structural metrics and the environmental covariates. For continuous predictors, we computed the area-weighted mean of covariate pixels intersecting each GEDI pixel. For discrete predictors (land cover types, aspect, and landform classes), we assigned the modal category across covariate pixels intersecting each GEDI pixel.

To reduce data volume, enable parallel processing, and lower computational burden (Kacic *et al* 2021, Potapov *et al* 2021), we segmented the study area into 2,108 tiles measuring 60 km by 60 km (figure 1) and used these tiles as the base units for local modeling. We arranged overlaps to improve consistency and reduce variability across adjacent tiles. Four neighboring tiles completely covered each tile (figure 2b), except tiles on the study area border. Within each tile, we randomly split GEDI observations into training (80%) and testing (20%) subsets, independently for the local RF model of each forest structural metric (figure 2d–f). We used the same percentages for all other model training and testing processes in this study. In addition, to tune the hyperparameters of RF models, we randomly sampled approximately 10 validation observations from each tile (see Supplementary material, section S3: Model hyperparameter tuning).

We then filtered the 60-km tiles based on the number and spatial distribution of GEDI observations. To ensure robust RF model training, we retained only tiles with at least 1,000 training observations, a threshold that exceeded 10 times the number of predictors. To improve spatial representativeness and avoid clustering near tile edges or corners, we required each tile to include at least 10% of its observations within a 30-km by 30-km grid cell centered on the tile centroid (figure 2b). The final set of local modeling units included 1,693 qualified tiles (figure 1), each with an average of approximately 14,582 GEDI observations (minimum 1,259; maximum 61,889). As one 30-m pixel could fall within up to four overlapping 60-km tiles, we combined n local RF predictions per pixel (n = 1 to 4) into a single prediction by accounting for each local RF model's predictive performance and the pixel's location within the overlapping tiles (see Supplementary material, section S4: Aggregating local predictions).

2.4. Predictor Contributions and Model Comparison

We evaluated contributions of the seven predictor groups for each forest structural metric using variable importance from the 1,693 local RF models. In each local model, we computed variable importance for all the 93 predictors, selected the top 20 covariates, and averaged their importance within each predictor group. For each local model, we identified the predictor group with the highest average top-20 importance as the local top predictor group for the corresponding forest

structural metric. This analysis accounted for differences in the number of covariates across predictor groups.

Local models restrict training to limited neighborhoods and can capture local patterns, limit extrapolation, and adapt to spatially varying predictor–response relationships (Fink *et al* 2010). In contrast, global models pool data across the full extent of a study region and increase the number and representativeness of training observations (Fink *et al* 2010, Potapov *et al* 2021). To evaluate the data-fusion performance of local models, we compared local and global RF models for predicting each forest structural metric from the environmental covariates (see Supplementary material, section S5: Local and global model comparison).

3. Results

3.1. Local Model Performance

Local RF models achieved variable predictive performance (R^2 and Root-Mean-Square Error (RMSE)) across the forest structural metrics (figure 3 and supplementary figure S6), especially between the footprint-level properties (canopy height, canopy cover, PAI, FHD; see Supplementary material, section S6: Local model predictions of footprint-level metrics) and the vertical layering metrics (PAVD and relative height difference (RHD)). Among the footprint-level metrics (figure 3), median local-model R^2 values reached 0.63 for canopy height, 0.63 for canopy cover, 0.54 for PAI, and 0.61 for FHD, indicating that local models explained more than 50% of the variation in these metrics in half of the 1,693 tiles. Spatially, local models performed relatively well in the Lower Great Lakes/St. Lawrence Plain, yielding an average median R^2 of 0.67 across the footprint-level properties (figure 4). The Piedmont followed closely with an average of 0.63. In contrast, average median R^2 was lower in the Appalachian Mountains (0.60) and the Atlantic Northern Forest (0.53). Among the PAVD metrics (figure 3), local model performance for the intermediate strata ($PAVD_{10–20m}$, median $R^2 = 0.55$; $PAVD_{20–30m}$, median $R^2 = 0.49$) was better than for the lowest ($PAVD_{0–10m}$, 0.32) and highest ($PAVD_{30–40m}$, 0.34) strata. For the RHD metrics (figure 3), the median R^2 value for the lowest range ($RHD_{25–50\%}$, 0.45) exceeded those for the upper ranges ($RHD_{50–75\%}$, 0.34; $RHD_{75–98\%}$, 0.25). Across most tiles, local models for $RHD_{75–98\%}$ explained about one quarter of the variation and showed the weakest predictive performance among all the forest structural metrics.

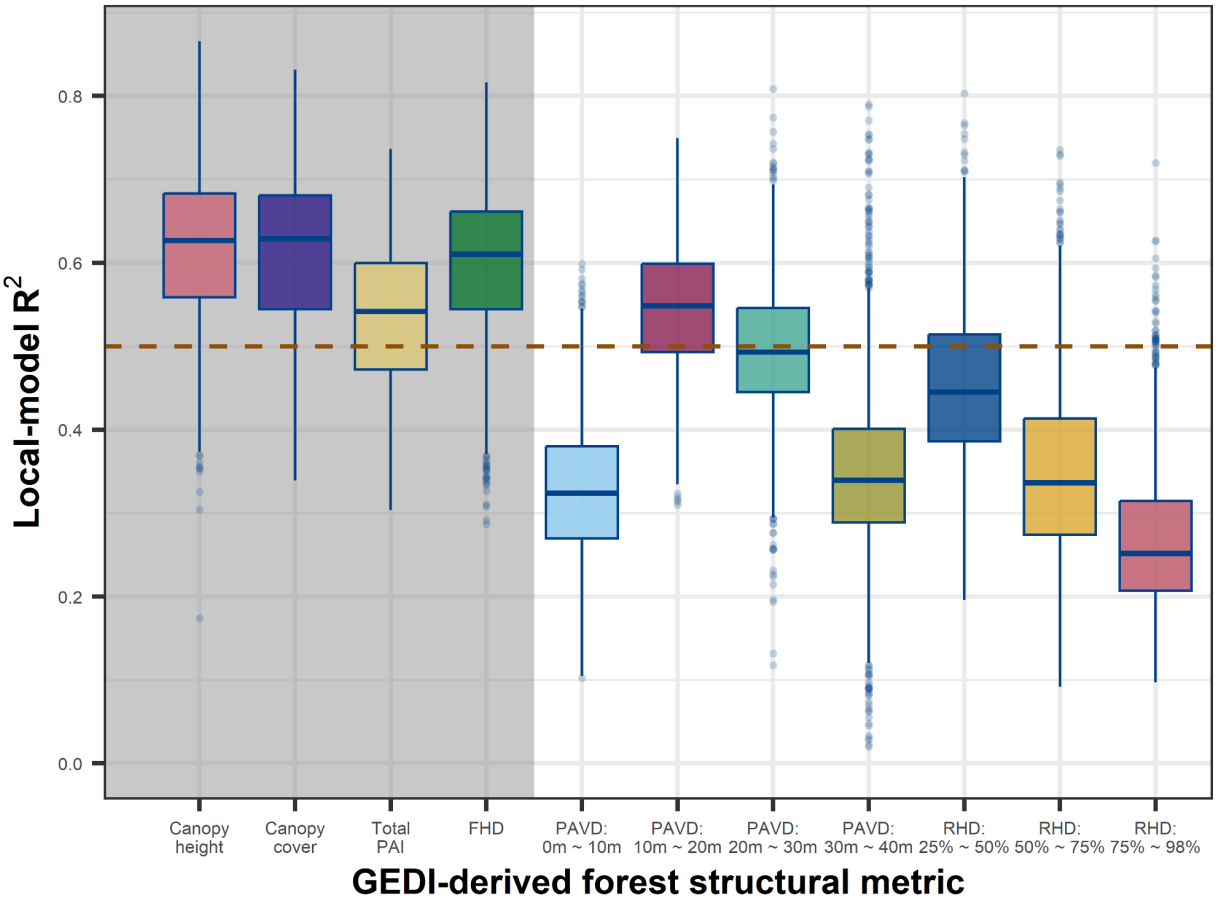

Figure 3. Local random forest models show variable predictive performance (R^2) across GEDI-derived forest structural metrics, with pronounced differences between footprint-level metrics (gray background) and vertical layering properties (no background). Metrics include canopy height, total canopy cover, total plant area index (PAI), foliage height diversity (FHD), plant area volume density (PAVD), and relative height difference (RHD). The dashed brown line marks $R^2 = 0.5$. We exclude five outliers with negative R^2 values for $PAVD_{30–40m}$ from the corresponding box plot to improve visualization clarity.

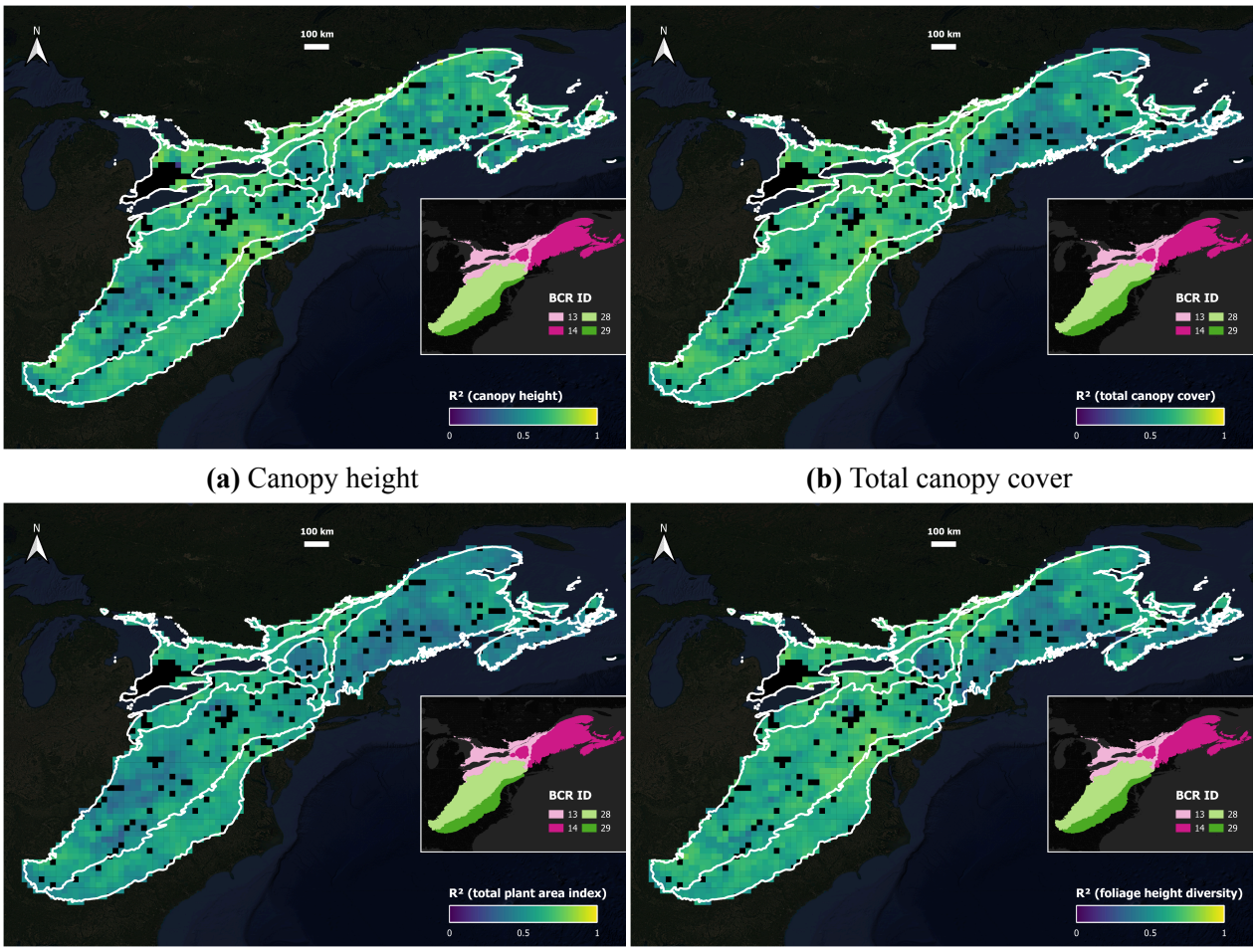

(a) Canopy height **(b)** Total canopy cover

(c) Total plant area index **(d)** Foliage height diversity

Figure 4. Local random forest models of footprint-level forest structural metrics show variable predictive performance (R^2) across the four Bird Conservation Regions (BCRs). Metrics include **(a)** canopy height, **(b)** total canopy cover, **(c)** total plant area index, and **(d)** foliage height diversity. We assign each local-model R^2 to the corresponding nonoverlapping 30-km grid cell for visualization. Black areas indicate regions outside the 30-km grid coverage. White polygons and inset maps delineate the four BCRs: Lower Great Lakes/St. Lawrence Plain (BCR 13), Atlantic Northern Forest (BCR 14), Appalachian Mountains (BCR 28), and Piedmont (BCR 29).

Local RF model predictions correlated strongly with observed values across all the forest structural metrics at the validation observations (Pearson's $r > 0.65$), but correlation strength varied by metric (figure 5). The footprint-level metrics, particularly canopy height ($r = 0.891$) and canopy cover (0.865), yielded relatively high correlation coefficients, consistent with the high R^2 values from their local models (figure 3). Among the vertical layering metrics, $PAVD_{10–20m}$ (0.857), $PAVD_{20–30m}$ (0.854), and $RHD_{25–50\%}$ (0.801) also showed relatively strong correlations (figure 5), aligning with the corresponding local model performance (figure 3). Despite the

overall strong correlations, the local models tended to overpredict low values and underpredict high values of the forest structural metrics (figure 5).

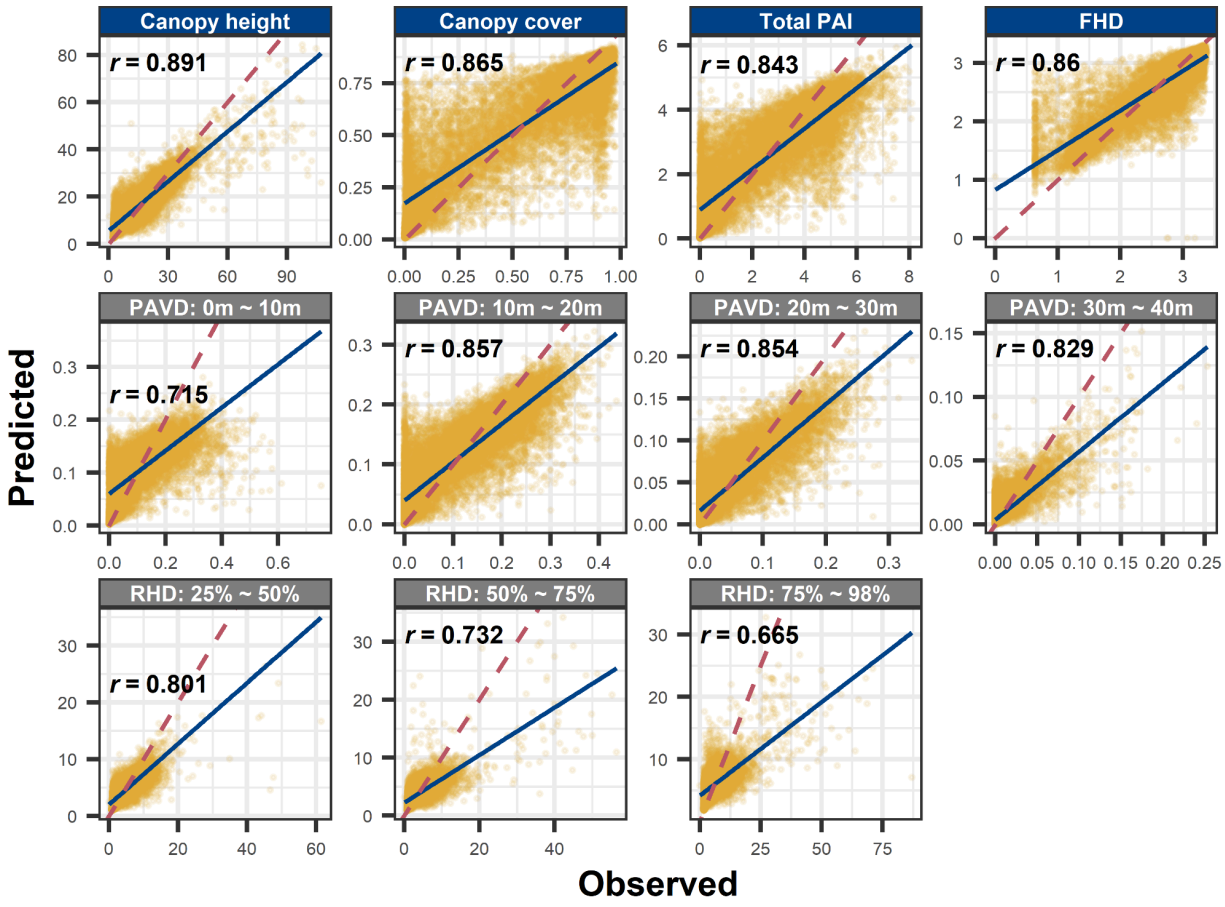

Figure 5. Local random forest model predictions show strong correlations (Pearson's $r > 0.65$) with observed values across all GEDI-derived forest structural metrics for 16,841 validation observations, although correlation strength varies by metric. Metrics include canopy height (unit: m), total canopy cover, total plant area index (PAI, unit: m^2/m^2), foliage height diversity (FHD), plant area volume density (PAVD, unit: m^2/m^3), and relative height difference (RHD, unit: m). Panels for footprint-level metrics have blue title bars. In each panel, the solid blue line shows the fitted trend between observed and predicted values, and the dashed red line marks the 1:1 line.

3.2. Top Predictor Groups

Environmental covariates derived from Sentinel-2 (S2), topography, and Landsat appeared as the top predictor groups in at least 69.6% of the 1,693 tiles for each forest structural metric (figure 6). Specifically, S2-based multispectral predictors ranked as the most common top predictor group for eight metrics: canopy cover (60.2% of tiles), PAI (58.1%), FHD (41.8%), $PAVD_{0–10m}$ (48.2%), $PAVD_{10–20m}$ (60.5%), $PAVD_{20–30m}$ (36.4%), $RHD_{25–50\%}$ (51.6%), and $RHD_{50–75\%}$ (42.9%). Topographic features served as the most common top predictor group for the remaining three

metrics, including canopy height (46.4%), $PAVD_{30–40m}$ (45.0%), and $RHD_{75–98\%}$ (38.4%). Landsat-derived multispectral covariates consistently ranked as the second or third most common top predictor group for most metrics, except for $PAVD_{30–40m}$, $RHD_{50–75\%}$, and $RHD_{75–98\%}$.

The distribution of top predictor groups varied with the level of local model performance for different forest structural metrics (figure 6). For the seven metrics with relatively high predictive performance of local RF models (median $R^2 > 0.4$), more than 85% of the tiles had top predictors belonging to the three most common groups: S2, topography, and Landsat. For the four metrics with relatively low local model performance (median $R^2 < 0.4$), a larger proportion of top predictors came from the remaining four less common groups, including Sentinel-1 (S1), land cover, leaf traits, and soil properties. These metrics included $PAVD_{0–10m}$ (19.2% from the less common groups), $PAVD_{30–40m}$ (30.4%), $RHD_{50–75\%}$ (24.5%), and $RHD_{75–98\%}$ (29.0%).

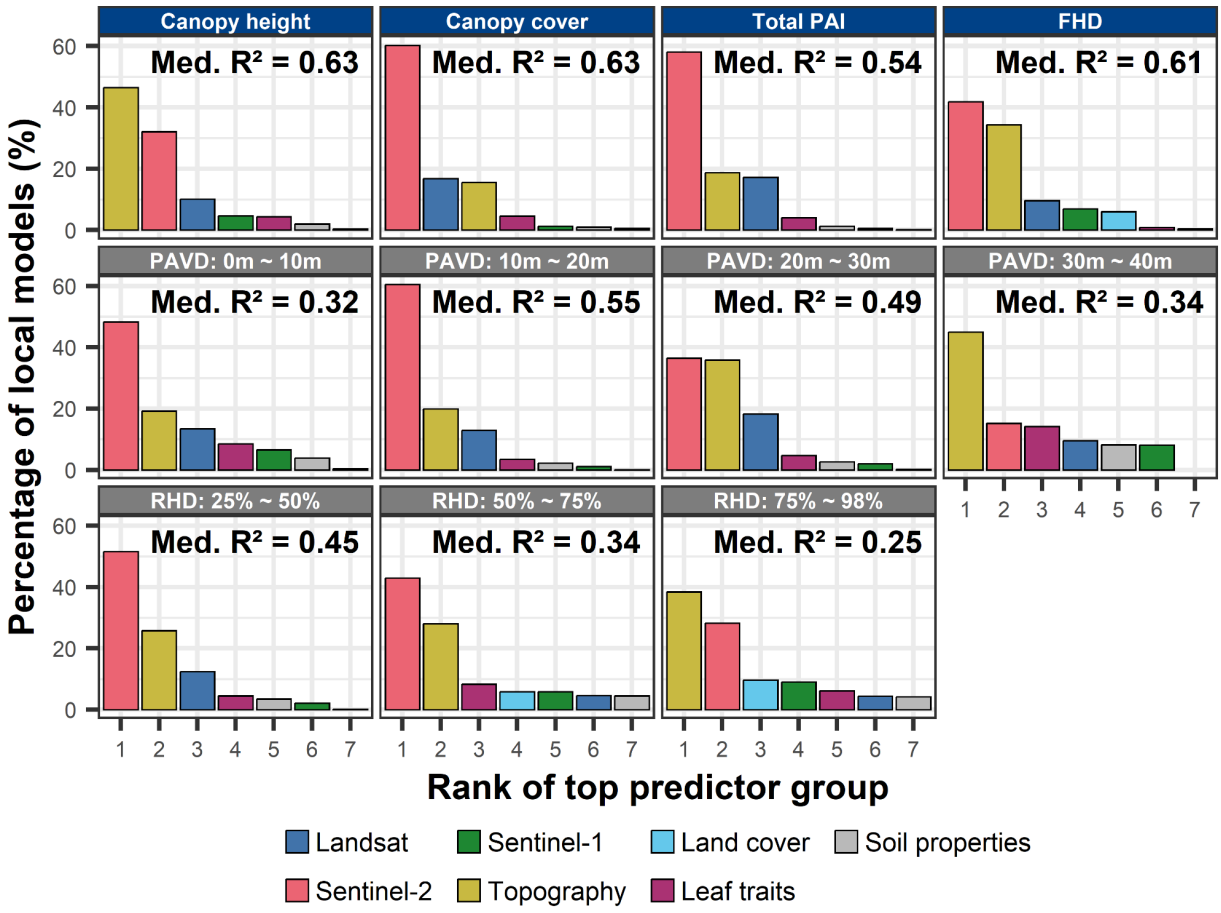

Figure 6. Environmental covariates from Sentinel-2, topography, and Landsat rank as the top predictor groups in most local random forest models for each GEDI-derived forest structural metric, and the distribution of top predictor groups varies with local model performance across metrics. Bars show the percentage of local models (60-km tiles) in which each predictor group ranks highest for a given metric: canopy height, total canopy cover, total plant area index (PAI), foliage height diversity (FHD), plant area volume density (PAVD), and relative height difference (RHD). Panels for footprint-level metrics have blue

title bars. For each metric, the median (med.) R^2 of the corresponding local models is shown.

Predictor contributions in local RF models for the footprint-level forest structural metrics (i.e., canopy height, canopy cover, PAI, and FHD) varied widely across the study area (figure 7). For canopy height and FHD, S2-based multispectral covariates contributed strongly in the Appalachian Mountains and the Piedmont in the southern portion of the study area (figure 7a,d). In contrast, topographic features played a greater role in the Lower Great Lakes/St. Lawrence Plain and the Atlantic Northern Forest in the north. For canopy cover and PAI, S2-derived predictors consistently made large contributions across all four BCRs (figure 7b,c). The Appalachian Mountains showed the only notable exception, where Landsat-derived multispectral covariates contributed more in some local models.

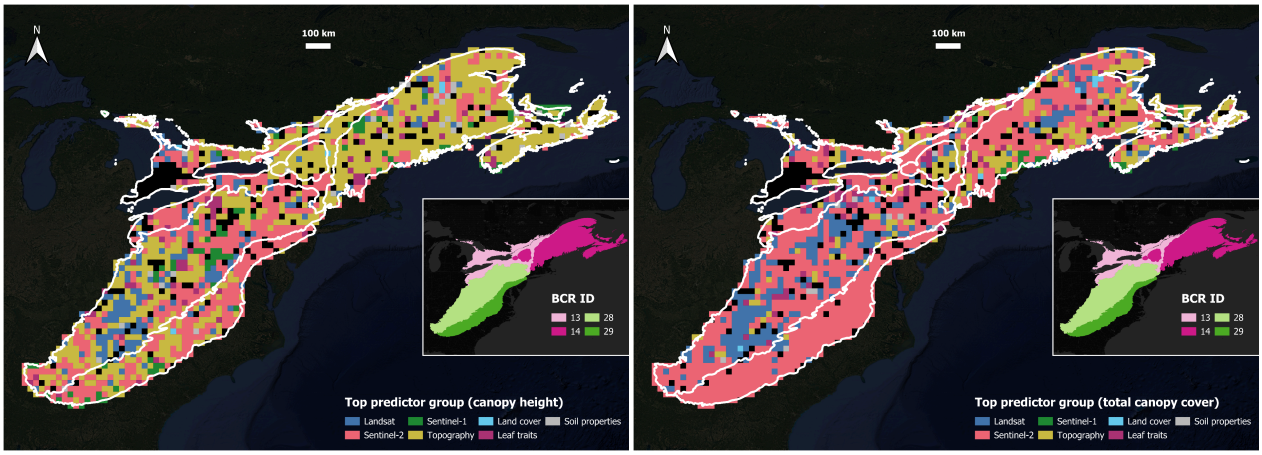

(a) Canopy height **(b)** Total canopy cover

(c) Total plant area index **(d)** Foliage height diversity

Figure 7. Predictor contributions from local random forest models for footprint-level forest structural metrics vary across the four Bird Conservation Regions (BCRs). Metrics include **(a)** canopy height, **(b)** total canopy cover, **(c)** total plant area index, and **(d)** foliage height diversity. We assign each local model's top predictor group to the corresponding nonoverlapping 30-km grid cell for visualization. Black areas indicate regions outside the 30-km grid coverage. White polygons and inset maps delineate the four BCRs:

Lower Great Lakes/St. Lawrence Plain (BCR 13), Atlantic Northern Forest (BCR 14), Appalachian Mountains (BCR 28), and Piedmont (BCR 29).

3.3. Comparison of Local and Global Models

Across the 11 forest structural metrics, local RF models outperformed the corresponding global RF models in a mean of 56.7% of the 30 sampled tiles (positive average $\Delta R^2_{s,i,m}$ in equation (6) of the Supplementary material; figure 8). Seven metrics exhibited better predictive performance for local models than for the corresponding global models in at least half of the sampled tiles. For all metrics except $PAVD_{0–10m}$, tiles with relatively poor global models (low average $R^2_{global,s,i,m}$ in equation (6) of the Supplementary material) more often favored local models. Across the 11 metrics (supplementary figure S7), local models more frequently achieved superior predictive performance (positive median value of the average $\Delta R^2_{s,i,m}$ across the sampled tiles) when the corresponding global models had relatively poor performance (low median value of the average $R^2_{global,s,i,m}$ across tiles). Among the nine metrics with relatively poor global models (median average $R^2_{global,s,i,m} < 0.5$), seven showed superior local models (median average $\Delta R^2_{s,i,m} > 0$). In contrast, canopy cover and FHD, which had stronger global models, did not gain from local models.

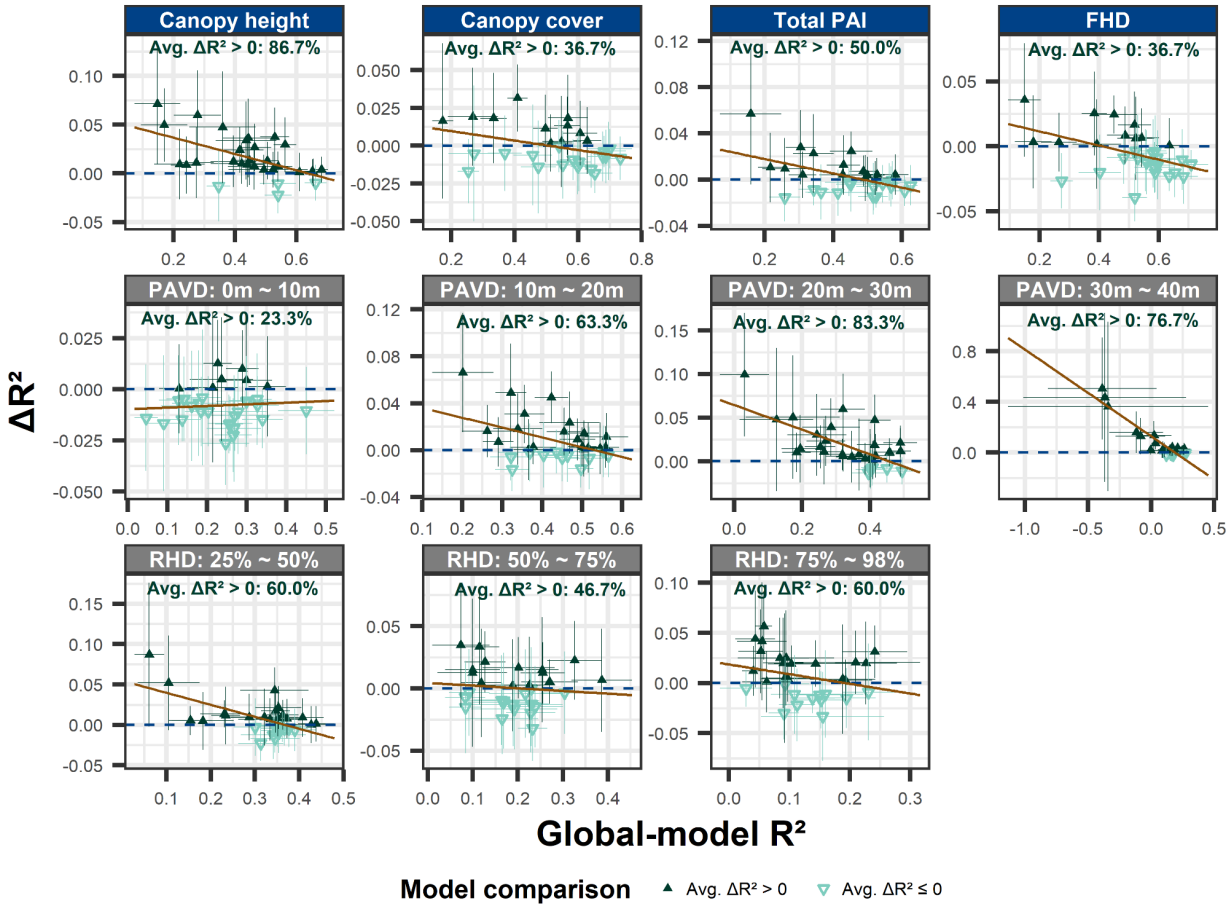

Figure 8. Local random forest models outperform the corresponding global random forest models in most of the 30 randomly sampled 60-km tiles, especially in tiles with relatively poor global models, for predicting the 11 GEDI-derived forest structural metrics: canopy height, total canopy cover, total plant area index (PAI), foliage height diversity (FHD), plant area volume density (PAVD), and relative height difference (RHD). Footprint-level metric panels use blue title backgrounds. Triangles and error bars show the mean and one standard deviation of global-model R^2 (x axis) and ΔR^2 (y axis, the R^2 difference between local and global models; see equation (6) in the Supplementary material). Dark green indicates tiles where average (avg.) ΔR^2 is positive, and light green indicates tiles where avg. ΔR^2 is nonpositive. The solid brown line shows the general trend between global-model R^2 and ΔR^2 for each metric, and the dashed blue line marks $\Delta R^2 = 0$. The panel for $PAVD_{30–40m}$ omits two tiles with global-model R^2 below −1 for clarity.

4. Discussion

In this study, we predicted 11 GEDI-derived forest structural metrics across eastern North America for 2019–2022 using a local data-fusion modeling framework based on 93 environmental covariates. Overall, the local RF models achieved strong correlations between predicted and observed GEDI measurements, though their predictive performance varied across metrics and regions. Local models performed generally well for the footprint-level metrics, which

was especially evident in the Lower Great Lakes/St. Lawrence Plain and the Piedmont, suggesting that the environmental covariates more effectively captured footprint-level forest structure in areas with less complex topography. Among the footprint-level metrics, canopy height and cover achieved the highest model accuracy, consistent with their widespread application for predicting forest characteristics at regional (Favrichon *et al* 2025, Schlickmann *et al* 2025, Seyrek *et al* 2025, Tamiminia *et al* 2024, Kacic *et al* 2023, Burns *et al* 2025, Vogeler *et al* 2023, Ngo *et al* 2023) and global scales (Potapov *et al* 2021, Lang *et al* 2023, Burns *et al* 2024). Second, across the fixed-stratum densities, models for $PAVD_{10–20m}$ and $PAVD_{20–30m}$ outperformed those for the lowest and highest strata. The relatively poor performance for the 0–10m stratum likely reflects the higher variability and reduced quality of near-ground GEDI returns during leaf-on conditions (Dhargay *et al* 2022, Vogeler *et al* 2023, Burns *et al* 2025). Similarly, sparse data coverage reduced model performance for the 30–40 m stratum, as few forest canopies in the study area exceeded 34 m. The saturation effect of GEDI signals in tall canopies likely increased the uncertainty in predicting structural properties in the upper range (Zhang *et al* 2024a). Third, among the relative height ranges, $RHD_{50–75\%}$ and $RHD_{75–98\%}$ models performed worse than those for $RHD_{25–50\%}$, likely due to greater structural complexity and variability of plant materials in the middle and upper canopy layers.

Local RF models showed differing covariate importance across forest structural metrics and predictor groups. Across all metrics, especially those with higher model performance, optical and topographic predictors consistently ranked among the most influential variables. S2-based optical features showed high importance in most local models, likely because their unique red-edge bands captured canopy properties and photosynthetic activity (Nasiri *et al* 2025, Aguirre-Gutiérrez *et al* 2021, Kacic *et al* 2023) and because their relatively fine spatial and temporal resolutions supported frequent, detailed observations (Copernicus n.d., Tamiminia *et al* 2024). In contrast, S1-derived SAR predictors ranked highly in fewer local models than optical and topographic covariates, despite the recognized value of SAR for surface vegetation analysis (Copernicus n.d., Schlund and Erasmi 2020, Mastro *et al* 2023, Nasirzadehdizaji *et al* 2019). This result aligns with earlier studies showing lower performance of S1 features in GEDI-based vegetation structure prediction compared to the predictors of S2 (Kacic *et al* 2021, Ziegler *et al* 2023, Ngo *et al* 2023, Kacic *et al* 2023), Landsat (Schlickmann *et al* 2025, Vogeler *et al* 2023), and topography (Kacic *et al* 2023). The short wavelength of C-band S1 SAR (~5.5 cm) likely reduced its ability to penetrate dense forest canopies (Ngo *et al* 2023). Long-wavelength SAR missions, such as L-band ~24-cm PALSAR-2 data (Ngo *et al* 2023, Sothe *et al* 2022) and the recently launched P-band BIOMASS mission (~69 cm, Quegan *et al* 2019), may address this limitation. Future research should also investigate additional radar-derived vegetation indices (e.g., Hu *et al* 2024), which may better capture forest structural variation than the limited SAR metrics used in this study.

Interestingly, despite their coarse spatial resolution (1 km), leaf traits ranked among the top predictors in a comparable proportion of local RF models as the 10-m S1 variables. This suggests that leaf-level characteristics were relevant to forest structure, possibly due to their relationships

with plant establishment, fitness, and survival (Moreno-Martínez *et al* 2018). Soil properties rarely ranked highest, likely due to their coarse resolution (250 m). Incorporating higher-resolution soil data, such as the 10-m gridded National Soil Survey Geographic Database for the United States and Island Territories, could improve their utility in future models. Finally, the limited importance of land cover covariates in most local models likely reflects the low categorical diversity within the study area, which is largely dominated by the "temperate broadleaf and mixed forests" biome (Dinerstein *et al* 2017). Future GEDI-based vegetation structure prediction conducted at broader spatial scales may capture a wider range of land cover categories, potentially increasing their relevance in the modeling process.

To improve GEDI-based prediction of forest structure, future studies should incorporate additional types of environmental predictors tailored to different regions or broader spatial scales. The relationship between plant diversity and forest structure (Hakkenberg and Goetz 2021, Marselis *et al* 2022) suggests that incorporating detailed data on plant species richness and composition, such as distinctions between trees and understory species, could offer greater insight into the vertical distribution of plant materials and enhance the prediction of vertical layering metrics. Climate and anthropogenic influences also play a critical role in shaping forest structure by affecting tree species composition and functional diversity (Li *et al* 2023, Ehbrecht *et al* 2021, Marselis *et al* 2022), and should be incorporated when modeling forest structure at continental or near-global scales. Finally, accounting for historical disturbance regimes is essential for capturing long-term forest structural dynamics (Favrichon *et al* 2025, Clark *et al* 2025, Vogeler *et al* 2023, Burns *et al* 2025, Rishmawi *et al* 2022, Kacic *et al* 2023), particularly in regions subject to frequent disturbances (Doyle *et al* 2025). Different disturbance agents influence specific canopy layers or plant species in different ways. For example, moderate-severity fires and wind or ice storms affect lower and upper canopy layers, respectively, while species-specific diseases create gaps by targeting individual trees (Atkins *et al* 2020). Accounting for multiple disturbance types could improve the delineation of forest structural components.

Unlike the commonly used global models in GEDI-based data-fusion studies (Rishmawi *et al* 2021, Ngo *et al* 2023, Vogeler *et al* 2023, Tamiminia *et al* 2024, Schlickmann *et al* 2025, Rishmawi *et al* 2022, Sothe *et al* 2022, Kacic *et al* 2023, Burns *et al* 2025), our local modeling framework offers three key advantages: lower computational burden, greater data utilization, and higher model performance (Kacic *et al* 2021, Potapov *et al* 2021, Fink *et al* 2010). By dividing the study area into smaller spatial units, we enabled parallel processing on the cloud computing platform, GEE, which enhanced computational efficiency and facilitated replication in other regions with varying extents and GEDI data availability. Second, unlike global models that often require spatial thinning of GEDI footprints to manage processing demands and to balance the data quality and spatial representativeness of training observations across large geographic extents (Schlickmann *et al* 2025, Vogeler *et al* 2023, Sothe *et al* 2022, Rishmawi *et al* 2022, 2021, Burns *et al* 2025), our local modeling framework used the full set of high-quality GEDI observations and their associated environmental predictors. This approach allowed us to allocate independent GEDI observations as local testing subsets, which improved the reliability of model performance

assessments and ensured that local models generalized well to new data (Schlickmann *et al* 2025). Finally, analysis of 30 randomly sampled tiles showed that local models outperformed their corresponding global models in most cases across all forest structural metrics. The performance gains occurred more frequently in tiles and for metrics where global models performed poorly, underscoring the advantage of our local modeling framework in capturing spatial heterogeneity and enhancing prediction accuracy across complex forested landscapes.

5. Conclusion

We showed that a local modeling framework that integrates spaceborne LiDAR with diverse environmental predictors generates continuous, fine-resolution predictions of temperate forest structure across eastern North America. Spatial variation in model performance and covariate importance underscores the value of incorporating local information rather than relying solely on global models. Extending this approach will further improve prediction of three-dimensional forest structure over large geographic extents worldwide, thereby enhancing the contribution of forest structural information to biodiversity assessments, habitat modeling, and estimates of forest carbon stocks from regional to global scales.

Data Availability

Code for all analyses is available on GitHub: https://github.com/AccountName/RepositoryName/tree/main/Eastern_North_America/GEE/GEDI_Data_Fusion. Access the GEDI-Inferred ForeST Structure (GIFTS) data product through an interactive web application: https://lidar-birds.projects.earthengine.app/view/gifts.

Supplementary Material

S1. GEDI Data Filtering

First, to confirm the suitability of each waveform for surface structure analysis and the effective operation of the L2B algorithm (Hofton and Blair 2019, Marselis *et al* 2022), we retained L2A observations with "quality_flag = 1" and L2B observations with both "l2b_quality_flag = 1" and "algorithm_run_flag = 1" (Schlickmann *et al* 2025, Rex *et al* 2025, Li *et al* 2024b, Burns *et al* 2024, Li *et al* 2024a, Seyrek *et al* 2025, Mohammadpour *et al* 2025, Kacic *et al* 2023). Second, to ensure accurate geolocation, we excluded any L2 measurements flagged with "degrade_flag ≠ 0", which indicates compromised pointing or positioning information (Dubayah *et al* 2022, Rishmawi *et al* 2021, Seyrek *et al* 2025, Mohammadpour *et al* 2025, Kacic *et al* 2023, Rishmawi *et al* 2022). Third, to minimize the influence of background solar illumination on waveform quality (Duncanson *et al* 2020, Hancock *et al* 2019), we included only nighttime observations (Li *et al* 2023, Schlickmann *et al* 2025, Favrichon *et al* 2025, Vogeler *et al* 2023, Beck *et al* 2021, Rishmawi *et al* 2022). Fourth, to address the limited canopy penetration of GEDI coverage beams (Beck *et al* 2021), we used data from full-power beams, which emit higher energy and thereby improve the likelihood of detecting reliable ground signals under dense canopy conditions (Duncanson *et al* 2020, Hancock *et al* 2019, Schlickmann *et al* 2025, Lahssini *et al* 2022, Li *et al* 2024a, Vogeler *et al* 2023, Ngo *et al* 2023, Sothe *et al* 2022). Finally, to reduce the occurrence of false positive ground returns, we retained only those GEDI shots with beam sensitivity values greater than 0.95 (Rishmawi *et al* 2021, Dubayah *et al* 2022, Crockett *et al* 2023, Dhargay *et al* 2022, Burns *et al* 2024, Seyrek *et al* 2025, Vogeler *et al* 2023, Li *et al* 2024b, Kacic *et al* 2023).

To further enhance the quality of the collected GEDI observations, we applied a series of additional filtering steps following recent recommendations for mapping global vegetation structural metrics (Burns *et al* 2024). Specifically, we retained only footprints with "surface_flag = 1", restricted "elev_lowestmode" values to the range of -200 to 9,000 meters to ensure reliable surface elevation measurements, and constrained the highest reflecting surface height (RH100) to values from 0 to 120 m to exclude unrealistic canopy heights. In addition, we removed observations located in areas with high levels of urban development or persistent surface water by applying the thresholds "urban_proportion < 50" and "landsat_water_persistence < 10".

Finally, we filtered the collected GEDI observations to include only those with plausible vegetation structural metrics, ensuring that: (a) total canopy cover fraction and vertical-profile values ranged from 0 to 1; (b) total PAI and vertical profile measurements were nonnegative; (c) plant area volume density (PAVD) for each 5-meter vertical interval was nonnegative; and (d) foliage height diversity (FHD) was nonnegative.

S2. Environmental Predictor Determination and Preprocessing

Groups 1 & 2: Landsat-8/9 and Sentinel-2 Imagery

We collected Landsat-8/9 and Sentinel-2 (S2) multispectral imagery from May through September, 2019–2022. Researchers have fused these data with GEDI observations to model vegetation structure across spatial scales (Favrichon *et al* 2025, Lang *et al* 2023, Vogeler *et al* 2023, Schlickmann *et al* 2025, Ziegler *et al* 2023, Tamiminia *et al* 2024, Ngo *et al* 2023, Seyrek *et al* 2025, Kacic *et al* 2023, Burns *et al* 2025). We obtained from GEE the NASA Harmonized Landsat and S2 project developed Landsat-8/9 data product (HLSL30) (Claverie *et al* 2018, Masek *et al* 2021) and applied the "Fmask" per-pixel quality assessment (QA) mask to reduce clouds and cloud shadows (Zhu *et al* 2015, Qiu *et al* 2019). We also obtained the Harmonized S2 Level-2A data product (Copernicus n.d.) from GEE. To identify relatively clear pixels and remove clouds and cloud shadows from S2 imagery, we used the "Cloud Score+" QA processor and excluded S2 pixels with a "cs" QA score below 0.5 (Pasquarella *et al* 2023).

We derived two types of environmental covariates from HLSL30 and S2 imagery: surface reflectance and spectral indices. First, we computed the median surface reflectance for each selected HLSL30 and S2 band at each pixel across all observations during 2019–2022. We then rescaled S2 data to 30 m by averaging pixel values with weights proportional to their overlap with 30-m pixels. Using the median surface reflectance, we calculated spectral indices at 30 m that assess vegetation properties and other environmental conditions. Among these indices, Normalized Difference Water Index reflects vegetation water content (Gao 1996), and Modified Normalized Difference Water Index targets open water detection (Xu 2006). Finally, we applied a tasseled cap transformation to extract the brightness, greenness, and wetness components from the multispectral data (Zhai *et al* 2022, Shi and Xu 2019).

Group 3: Radar Data

We collected Sentinel-1 (S1) Ground Range Detected scenes in "Interferometric Wide" swath mode through GEE (Copernicus n.d., Anon n.d.). These data support forest type classification, biomass estimation, and disturbance detection (Copernicus n.d.). First, we extracted the cross-polarized vertical-horizontal and the co-polarized vertical-vertical backscattering coefficients at 10-m resolution from May to September during 2019–2022 (Vogeler *et al* 2023, Tamiminia *et al* 2024, Kacic *et al* 2021, Ziegler *et al* 2023, Schlickmann *et al* 2025, Nasiri *et al* 2025, Ngo *et al* 2023, Kacic *et al* 2023, Sothe *et al* 2022). Second, we calculated the pixelwise median of each coefficient across all observations in the study period. Third, we derived three radar indices at 10-m resolution from the median coefficient values to assess phenological, physiological, and structural characteristics of surface vegetation (Kim and van Zyl 2004, 2009, Hu *et al* 2024, Copernicus n.d., Schlund and Erasmi 2020, Mastro *et al* 2023, Schlickmann *et al* 2025, Vogeler *et al* 2023, Ngo *et al* 2023). Last, we aggregated the median coefficient values and the radar indices to 30-m resolution by area-weighted averaging of overlapping S1 pixels.

Group 4: Land Cover Information

We used two annual data products for 2019–2022 to capture spatial land cover variation within the study area and to evaluate relationships with forest structure (Kacic *et al* 2021, 2023, Rishmawi *et al* 2022, 2021): (a) the 10-m S2-based land cover dataset, which includes nine classes (Karra *et al* 2021), and (b) the 30-m Landsat-based land cover dataset, which includes 35 classes (Zhang *et al* 2024b, Liu *et al* 2023). The S2-based dataset contains a general "trees" category, while the Landsat-based dataset separates forested areas into 10 categories, which enables a more detailed classification of forest types. For each product, we identified the most frequent land cover class for each pixel across 2019–2022 and assigned the dominant S2-based category to each 30-m pixel. We then removed pixels labeled "water" or "water body" to avoid mischaracterizing forest structure in those areas (Vogeler *et al* 2023).

Group 5: Topographic Features

We used the ALOS World 3D-30m (AW3D30) global digital surface model Version 3.2 (Takaku *et al* 2016, 2020, Tadono *et al* 2016) to represent topographic gradients across the study domain. Relative to other freely available global DEMs (e.g., ASTER, MERIT, TanDEM-X, SRTM, NASADEM), AW3D30 showed lower uncertainty and higher accuracy (Uuemaa *et al* 2020) and matched the spatial resolution of the GEDI data-fusion results. We derived elevation, slope, aspect, and indices of east-westness and north-southness (Sherman *et al* 2008, Wilson *et al* 2015) from AW3D30. We also retrieved four AW3D30-based topographic features from GEE: (a) 90-m landform classes, (b) 90-m Continuous Heat-Insolation Load Index (CHILI), (c) 270-m topographic diversity, and (d) 270-m multi-scale Topographic Position Index (mTPI) (Theobald *et al* 2015). To match the target spatial resolution, we resampled the numeric features (CHILI, topographic diversity, mTPI) to 30 m with bilinear interpolation and the categorical feature (landform classes) with the nearest-neighbor algorithm.

Groups 6 & 7: Leaf Traits and Soil Properties

We included leaf traits and soil properties to capture their potential relationships with forest structure, given their associations with tree species composition and functional diversity (Kacic *et al* 2021, Ehbrecht *et al* 2021). We first used a 1-km remote-sensing- and climate-informed leaf trait dataset that provides estimates of specific leaf area, leaf dry matter content, leaf nitrogen content per dry mass, and leaf phosphorus content per dry mass for terrestrial vegetated areas, excluding fern and crop species (Moreno-Martínez *et al* 2018). Second, we extracted 10 key properties from a 250-m soil dataset (Poggio *et al* 2021) across three layers (0–5 cm, 5–15 cm, and 15–30 cm): (a) bulk density of the fine earth fraction, (b) cation exchange capacity of the soil, (c) volumetric fraction of coarse fragments (> 2 mm), (d) proportion of clay particles (< 0.002 mm) in the fine earth fraction, (e) total nitrogen, (f) soil pH, (g) proportion of sand particles (> 0.05 mm) in the fine earth fraction, (h) proportion of silt particles (≥ 0.002 mm and ≤ 0.05 mm) in the fine earth fraction, (i) soil organic carbon content in the fine earth fraction, and (j) organic

carbon density. We also included organic carbon stocks for the full 0–30 cm topsoil layer. We resampled all leaf trait and soil property variables to 30-m resolution using the bilinear interpolation approach.

S3. Model Hyperparameter Tuning

Using 16,841 validation observations, we first identified the optimal number of decision trees (1 to 200) for RF models by selecting the smallest value beyond which Root-Mean-Square Error (RMSE) across all forest structural metrics stabilized (supplementary figure S1). Next, for each metric's RF models, we tuned three hyperparameters within predefined ranges: (a) number of variables per split (1 to 93), (b) minimum population in a leaf node (1 to 100), and (c) fraction of input data used for "bagging" per decision tree (1% to 99%). We conducted three independent tuning rounds per metric (supplementary figures S2-4). In each round, we adjusted one hyperparameter at a time to minimize RMSE and used different randomization seeds across candidate values to ensure robustness. For each metric, we adopted the third-round values as the final hyperparameters and used them to train the corresponding local RF models.

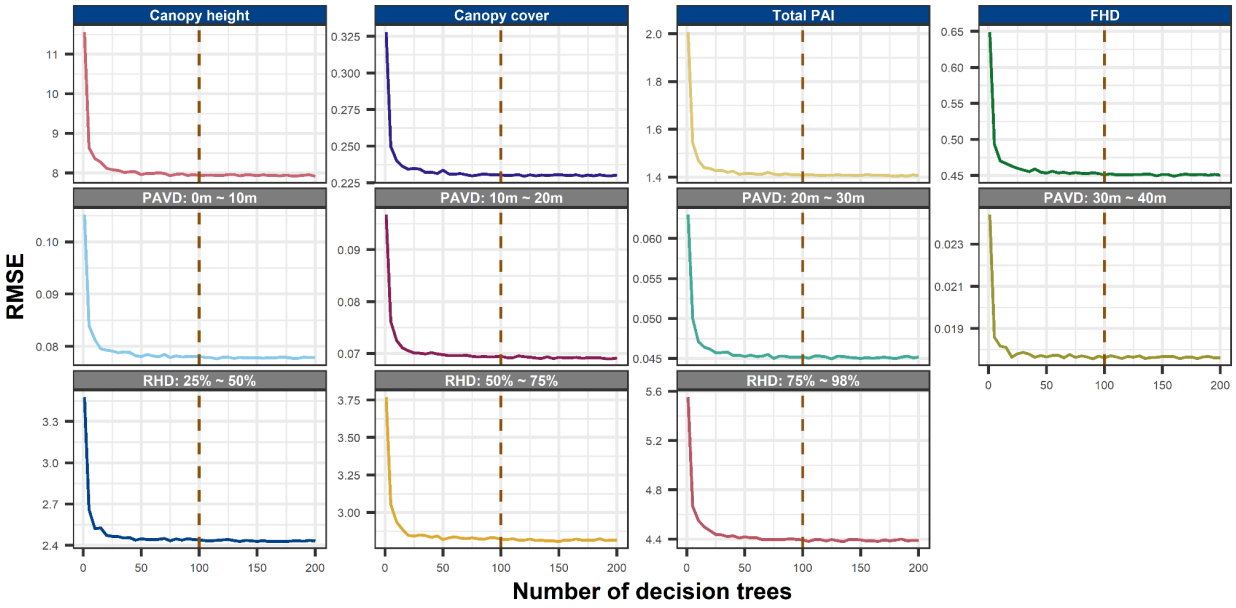

Supplementary Figure S1. Determination of the optimal number of decision trees for random forest models using 16,841 validation observations. Root-Mean-Square Error (RMSE) across all GEDI-derived forest structural metrics stabilizes beyond the chosen number between 1 and 200. Metrics include canopy height (unit: m), total canopy cover, total plant area index (PAI, unit: m^2/m^2), foliage height diversity (FHD), plant area volume density (PAVD, unit: m^2/m^3), and relative height difference (RHD, unit: m). Panels for footprint-level metrics have blue title bars. For each metric, the dashed brown line marks the selected number of decision trees (100).

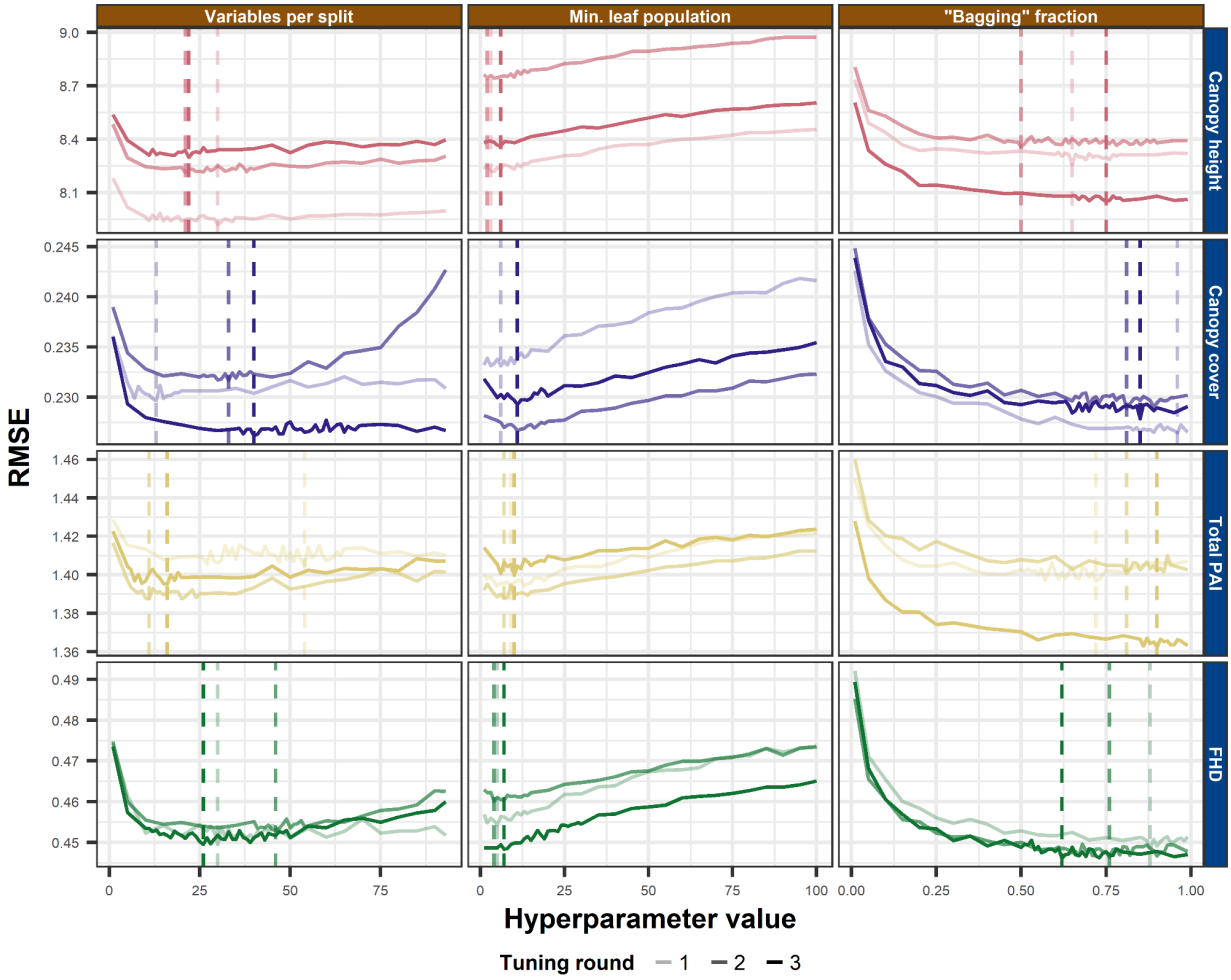

Supplementary Figure S2. Hyperparameter tuning for random forest models of footprint-level GEDI-derived forest structural metrics using 16,841 validation observations. Metrics include canopy height (unit: m), total canopy cover, total plant area index (PAI, unit: m^2/m^2), and foliage height diversity (FHD). In each panel, solid lines show Root-Mean-Square Error (RMSE) and vertical dashed lines mark the optimal value of the hyperparameter in each of three independent tuning rounds; line transparency indicates the round number. Third-round optima (least transparent lines) define the final hyperparameters for training the corresponding local random forest models for each metric.

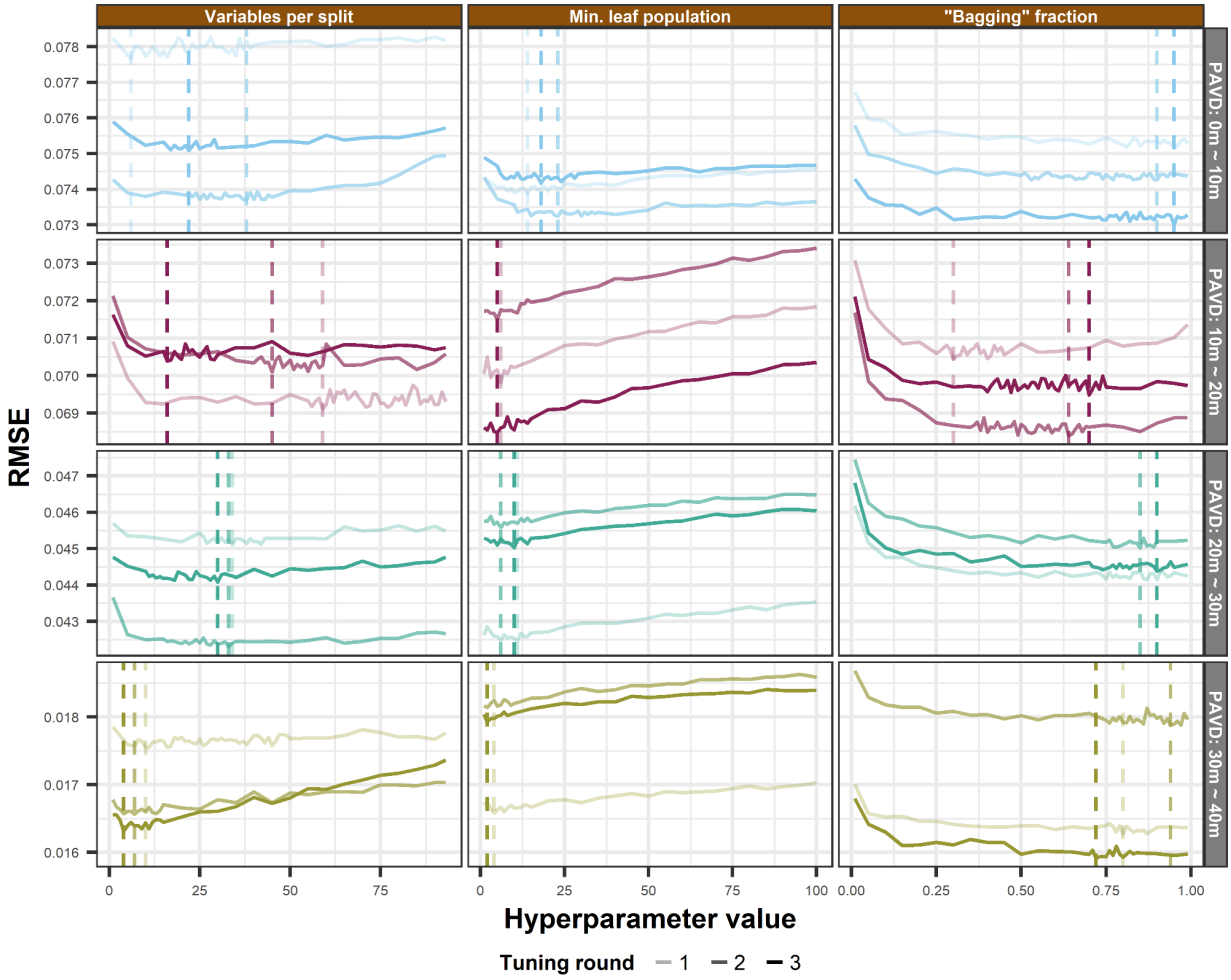

Supplementary Figure S3. Hyperparameter tuning for random forest models of GEDI-derived plant area volume density (PAVD, unit: m^2/m^3) metrics using 16,841 validation observations. In each panel, solid lines show Root-Mean-Square Error (RMSE) and vertical dashed lines mark the optimal value of the hyperparameter in each of three independent tuning rounds; line transparency indicates the round number. Third-round optima (least transparent lines) define the final hyperparameters for training the corresponding local random forest models for each metric.

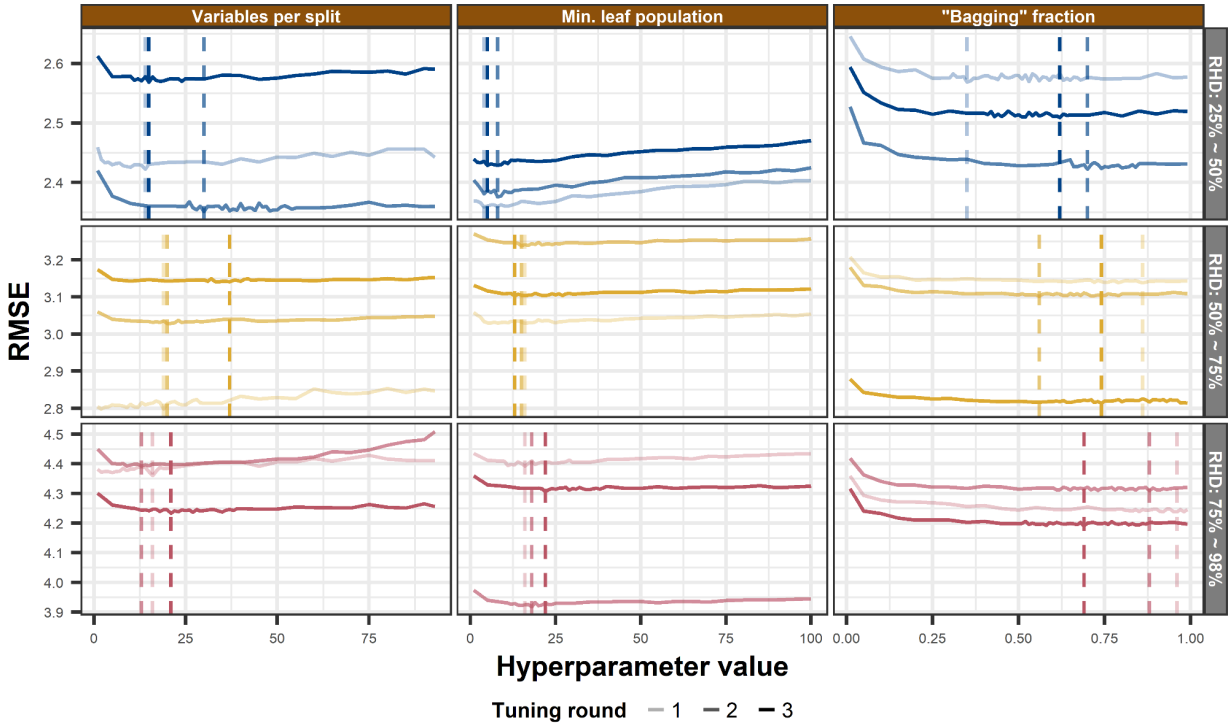

Supplementary Figure S4. Hyperparameter tuning for random forest models of GEDI-derived relative height difference (RHD, unit: m) metrics using 16,841 validation observations. In each panel, solid lines show Root-Mean-Square Error (RMSE) and vertical dashed lines mark the optimal value of the hyperparameter in each of three independent tuning rounds; line transparency indicates the round number. Third-round optima (least transparent lines) define the final hyperparameters for training the corresponding local random forest models for each metric.

S4. Aggregating Local Predictions

A 30-m pixel could fall within up to four overlapping 60-km tiles. We combined n local RF predictions per pixel (n = 1 to 4) into a single prediction by accounting for each local RF model's predictive performance and the pixel's location within the overlapping tiles. First, we calculated the inverse (I_t) of the Mean Squared Error (MSE_t) for the local model of the t-th tile (equation (1), where t ranges from 1 to n). We then normalized this value across all tiles using the minimum (I_{max}) and maximum (I_{min}) inverse MSE values (equation (2)).

$$I_t = MSE_t^{-1} \quad (1)$$

$$w_{MSE,t} = \frac{I_t - I_{min}}{I_{max} - I_{min}} \quad (2)$$

Second, we computed the Euclidean distance ($d_{p,t}$) from the p-th pixel to the geometric centroid of the t-th tile. We inverted and normalized this distance using the minimum (d_{min}, at the tile centroid) and maximum (d_{max}, at the tile corners) distances:

$$w_{d,p,t} = \frac{d_{max} - d_{p,t}}{d_{max} - d_{min}} \tag{3}$$

Third, we multiplied the normalized accuracy weight and distance weight to compute a composite weight ($w_{p,t}$) for each pixel-tile pair (equation (4)). This weight increased when the t-th tile showed higher model accuracy (lower MSE_t) and the p-th pixel lied closer to the tile centroid (lower $d_{p,t}$). We used these weights to compute the weighted mean of the n local RF predictions ($\widehat{\theta_{p,t}}$) at each pixel (equation (5)), where Z denotes the integers.

$$w_{p,t} = w_{MSE,t} \cdot w_{d,p,t} \tag{4}$$

$$\widehat{\theta_p} = \frac{\sum_{t=1}^{n} w_{p,t} \cdot \widehat{\theta_{p,t}}}{\sum_{t=1}^{n} w_{p,t}},\ n \in [1,\ 4] \cap Z \tag{5}$$

Finally, we evaluated the accuracy of the aggregated local RF predictions ($\widehat{\theta_p}$) against the corresponding GEDI measurements at the validation observations.

S5. Local and Global Model Comparison

We randomly sampled 30 nonoverlapping tiles (figure 1), each with at least 12,500 GEDI observations. For each tile, to account for model uncertainty, we drew 10 sets of 1,250 GEDI observations without replacement and trained a local RF model for each forest structural metric on each set. We also trained a global RF model for each metric using each observation set pooled across all 30 tiles. This design gave each local model an equal and adequate number of distinct GEDI observations within and across tiles and kept the number of observations for each global model within the GEE computational limit.

For the m-th forest structural metric (m = 1 to 11) within the i-th sampled tile (i = 1 to 30), we tested the local RF model and the corresponding global RF model on the same held-out testing set s (s = 1 to 10) and computed the R^2 difference:

$$\Delta R^2_{s,i,m} = R^2_{local,s,i,m} - R^2_{global,s,i,m},\ s \in [1,\ 10] \cap Z,\ i \in [1,\ 30] \cap Z,\ m \in [1,\ 11] \cap Z. \tag{6}$$

Here, s, i, and m index observation sets, sampled tiles, and forest structural metrics, respectively; Z denotes the integers. We treated $\Delta R^2_{s,i,m} > 0$ as evidence that the local model outperformed the global model. For each forest structural metric, within each sampled tile, we computed the mean and standard deviation of $\Delta R^2_{s,i,m}$ and $R^2_{global,s,i,m}$ across the 10 observation sets. We then summarized across the 30 sampled tiles by taking the median of the within-tile means for $\Delta R^2_{s,i,m}$ and $R^2_{global,s,i,m}$. This procedure quantified how performance differences between local and global models varied among the forest structural metrics.

S6. Local Model Predictions of Footprint-Level Metrics

Among the footprint-level forest structural metrics predicted by local RF models (supplementary figure S5; see the interactive web application under Data Availability), canopy height, canopy cover, and PAI decreased with increasing latitude across the study area. Canopy height ranged from 2.6 m to 40 m, with most forests measuring between 10 m and 26 m (supplementary figure S5a). Taller forests appeared primarily in the Appalachian Mountains, while shorter forests were more common in the Lower Great Lakes/St. Lawrence Plain and the northeastern Atlantic Northern Forest. Canopy cover ranged from 0.01 to 0.9 (supplementary figure S5b). We observed more forests with high canopy cover (greater than 0.5) in the Appalachian Mountains and the southwestern Atlantic Northern Forest. In contrast, more forests with low canopy cover (lower than 0.5) occurred in the Piedmont and the northeastern Atlantic Northern Forest. PAI showed a clear south-to-north decrease, especially in the Appalachian Mountains and the Atlantic Northern Forest (supplementary figure S5c). Its values dropped from above 3 m^2/m^2 in the Appalachian Mountains, indicating denser forests, to below 1.5 m^2/m^2 in the northeastern Atlantic Northern Forest, indicating sparser forests. Unlike the other footprint-level metrics, FHD did not show a pronounced latitudinal gradient (supplementary figure S5d). Its values ranged from 1.3 to 3.3 across the study area and reflected a relatively narrow range of forest structural heterogeneity. Most high values (above 2.5) occurred in the Appalachian Mountains and the southwestern Atlantic Northern Forest.

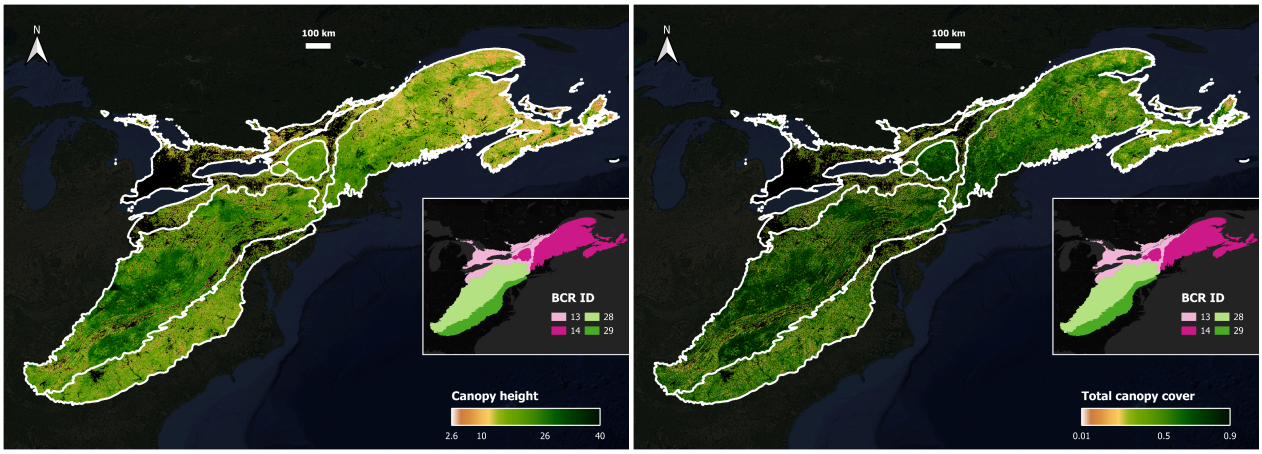

(a) Canopy height

(b) Total canopy cover

(c) Total plant area index

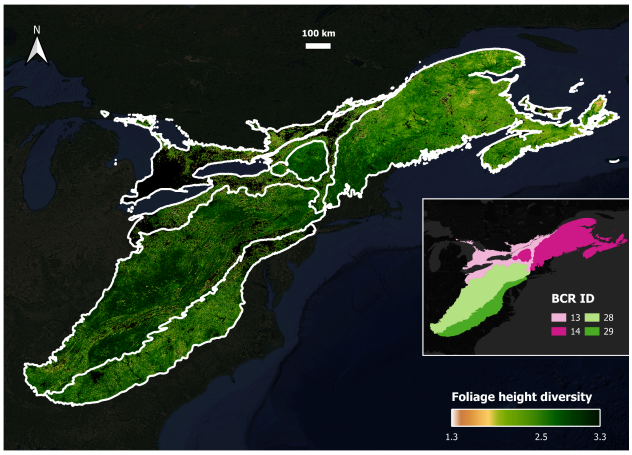

(d) Foliage height diversity

Supplementary Figure S5. Local model predictions of footprint-level forest structural metrics show latitudinal gradients, except for foliage height diversity. Metrics include **(a)** canopy height (unit: m), **(b)** total canopy cover, **(c)** total plant area index (unit: m^2/m^2), and **(d)** foliage height diversity. Maps display predictions at 300-m resolution for visualization. Black areas mark non-forested regions without predictions. White polygons and inset maps delineate the four Bird Conservation Regions (BCRs) in this study: Lower Great Lakes/St. Lawrence Plain (BCR 13), Atlantic Northern Forest (BCR 14), Appalachian Mountains (BCR 28), and Piedmont (BCR 29).

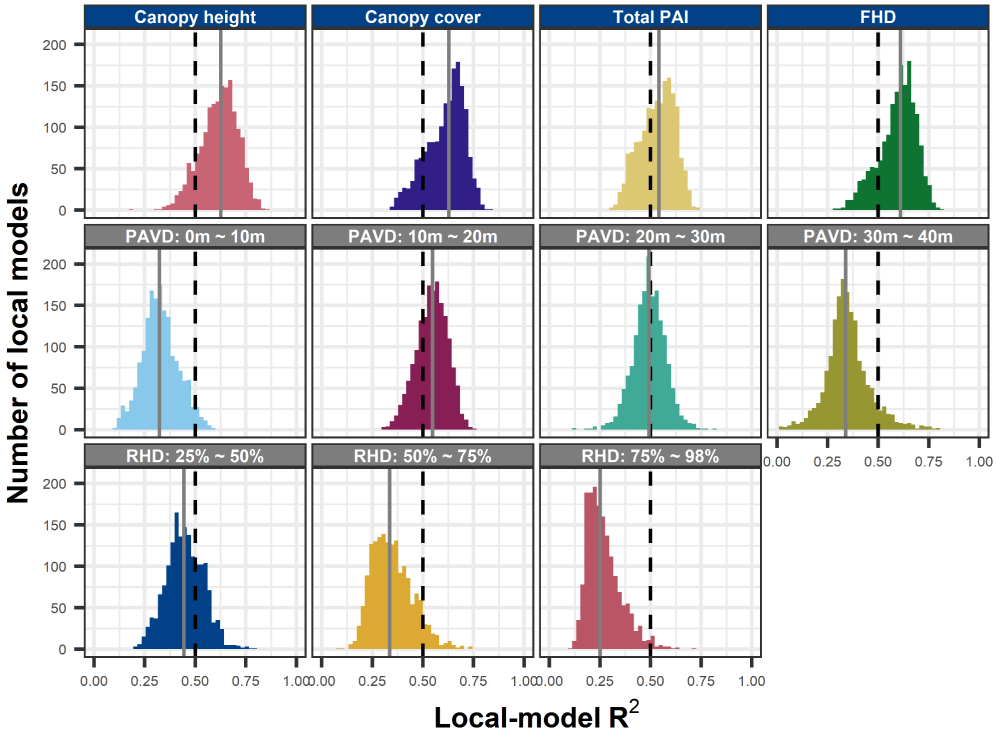

(a) Local-model R^2

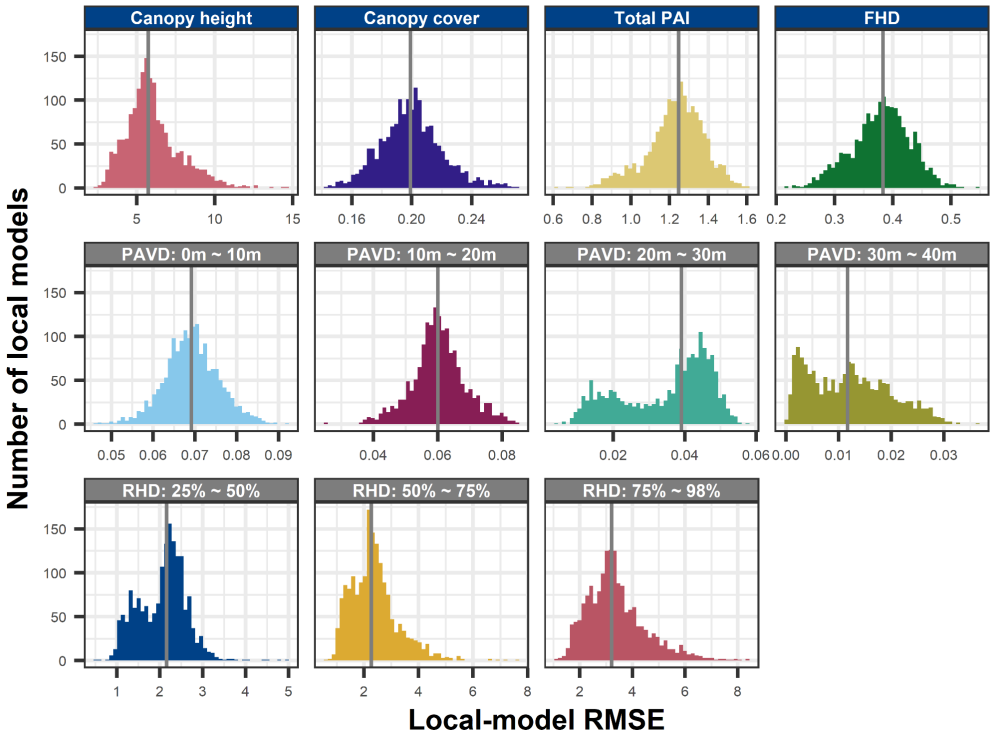

(b) Local-model RMSE

Supplementary Figure S6. Local random forest models show variable predictive performance (R^2 and Root-Mean-Square Error/RMSE) across GEDI-derived forest structural metrics. Metrics include canopy

height (unit: m), total canopy cover, total plant area index (PAI, unit: m^2/m^2), foliage height diversity (FHD), plant area volume density (PAVD, unit: m^2/m^3), and relative height difference (RHD, unit: m). Panels for footprint-level metrics have blue title bars. For each metric, the solid gray lines show the median (a) R^2 and (b) RMSE of the corresponding local models; the dashed black line marks $R^2 = 0.5$. To improve clarity, we exclude five outliers with negative R^2 values for $PAVD_{30–40m}$ from the corresponding histogram.

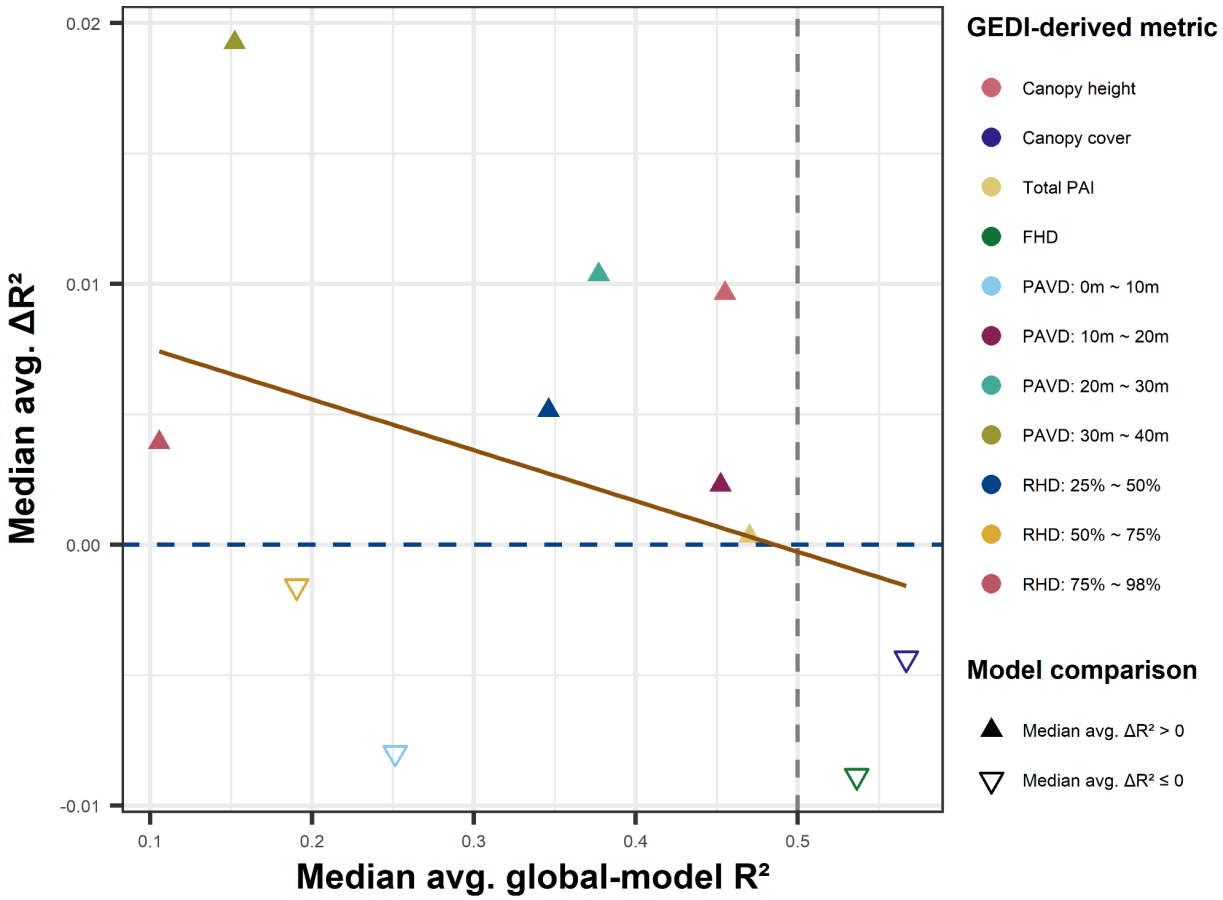

Supplementary Figure S7. Local random forest models more frequently achieve superior predictive performance across 30 randomly sampled 60-km tiles for the 11 GEDI-derived forest structural metrics when the corresponding global random forest models perform relatively poorly. Metrics include canopy height, total canopy cover, total plant area index (PAI), foliage height diversity (FHD), plant area volume density (PAVD), and relative height difference (RHD). Filled triangles indicate metrics with positive median values of the average (avg.) ΔR^2 across the sampled tiles; unfilled triangles indicate nonpositive median values. ΔR^2 denotes the R^2 difference between local and global models (equation (6)). The dashed gray vertical line marks a median value of 0.5 across the avg. global-model R^2 for the sampled tiles. The solid brown line depicts the trend between median avg. global-model R^2 and median avg. ΔR^2 across metrics, and the dashed blue horizontal line marks median avg. $\Delta R^2 = 0$.

References

Aguirre-Gutiérrez J, Rifai S, Shenkin A, Oliveras I, Bentley L P, Svátek M, Girardin C A J, Both S, Riutta T, Berenguer E, Kissling W D, Bauman D, Raab N, Moore S, Farfan-Rios W, Figueiredo A E S, Reis S M, Ndong J E, Ondo F E, N'ssi Bengone N, Mihindou V, Moraes de Seixas M M, Adu-Bredu S, Abernethy K, Asner G P, Barlow J, Burslem D F R P, Coomes D A, Cernusak L A, Dargie G C, Enquist B J, Ewers R M, Ferreira J, Jeffery K J, Joly C A, Lewis S L, Marimon-Junior B H, Martin R E, Morandi P S, Phillips O L, Quesada C A, Salinas N, Schwantes Marimon B, Silman M, Teh Y A, White L J T and Malhi Y 2021 Pantropical modelling of canopy functional traits using Sentinel-2 remote sensing data *Remote Sens. Environ.* **252** 112122

Anon Sentinel-1 Algorithms *Google for Developers* Online: https://developers.google.com/earth-engine/guides/sentinel1

Atkins J W, Bond-Lamberty B, Fahey R T, Haber L T, Stuart-Haëntjens E, Hardiman B S, LaRue E, McNeil B E, Orwig D A, Stovall A E L, Tallant J M, Walter J A and Gough C M 2020 Application of multidimensional structural characterization to detect and describe moderate forest disturbance *Ecosphere* **11** e03156

Atkins J W, Fahey R T, Hardiman B S and Gough C M 2018 Forest canopy structural complexity and light absorption relationships at the subcontinental scale *J. Geophys. Res. Biogeosci.* **123** 1387–405

Badgley G, Field C B and Berry J A 2017 Canopy near-infrared reflectance and terrestrial photosynthesis *Sci Adv* **3** e1602244

Bakx T R M, Koma Z, Seijmonsbergen A C and Kissling W D 2019 Use and categorization of Light Detection and Ranging vegetation metrics in avian diversity and species distribution research *Divers. Distrib.* **25** 1045–59

Beck J, Wirt B, Armston J, Hofton M, Luthcke S and Tang H 2021 GLOBAL Ecosystem Dynamics Investigation (GEDI) Level 2 User Guide *NASA EOSDIS Land Processes Distributed Active Archive Center* Online: https://lpdaac.usgs.gov/documents/986/GEDI02_UserGuide_V2.pdf

Belgiu M and Drăguţ L 2016 Random forest in remote sensing: A review of applications and future directions *ISPRS J. Photogramm. Remote Sens.* **114** 24–31

Breiman L 2001 Random Forests *Mach. Learn.* **45** 5–32

Burns P, Clark M, Salas L, Hancock S, Leland D, Jantz P, Dubayah R and Goetz S J 2020 Incorporating canopy structure from simulated GEDI lidar into bird species distribution models *Environ. Res. Lett.* **15** 095002

Burns P, Hakkenberg C R and Goetz S J 2024 Multi-resolution gridded maps of vegetation structure from GEDI *Sci. Data* **11** 881

Burns P, Kaszta Z, Cushman S A, Brodie J F, Hakkenberg C R, Jantz P, Deith M, Luskin M S, Ball J G C, Mohd-Azlan J, Burslem D F R P, Cheyne S M, Haidir I, Hearn A J, Slade E, Williams P J, Macdonald D W and Goetz S J 2025 The utility of dynamic forest structure from GEDI lidar fusion in tropical mammal species distribution models *Front. Remote Sens.* **6** 1563430

Camacho L F, Schwartz N and Avilés L 2025 Vegetation structural complexity across elevational gradients: Insights from the tropical Andes *J. Biogeogr.* Online:

https://onlinelibrary.wiley.com/doi/abs/10.1111/jbi.15102

Camps-Valls G, Campos-Taberner M, Moreno-Martínez Á, Walther S, Duveiller G, Cescatti A, Mahecha M D, Muñoz-Marí J, García-Haro F J, Guanter L, Jung M, Gamon J A, Reichstein M and Running S W 2021 A unified vegetation index for quantifying the terrestrial biosphere *Sci Adv* **7** Online: http://dx.doi.org/10.1126/sciadv.abc7447

Clark M L, Hakkenberg C R, Bailey T, Burns P and Goetz S J 2025 Changes in GEDI-based measures of forest structure after large California wildfires relative to pre-fire conditions *Remote Sens. Environ.* **323** 114718

Claverie M, Ju J, Masek J G, Dungan J L, Vermote E F, Roger J-C, Skakun S V and Justice C 2018 The Harmonized Landsat and Sentinel-2 surface reflectance data set *Remote Sens. Environ.* **219** 145–61

de Conto T, Armston J and Dubayah R 2024 Characterizing the structural complexity of the Earth's forests with spaceborne lidar *Nat. Commun.* **15** 8116

Copernicus S1 Applications *SentiWiki* Online: https://sentiwiki.copernicus.eu/web/s1-applications

Copernicus S1 Products *SentiWiki* Online: https://sentiwiki.copernicus.eu/web/s1-products

Copernicus S2 Products *SentiWiki* Online: https://sentiwiki.copernicus.eu/web/s2-products

Crockett E T H, Atkins J W, Guo Q, Sun G, Potter K M, Ollinger S, Silva C A, Tang H, Woodall C W, Holgerson J and Xiao J 2023 Structural and species diversity explain aboveground carbon storage in forests across the United States: Evidence from GEDI and forest inventory data *Remote Sens. Environ.* **295** 113703

Dhargay S, Lyell C S, Brown T P, Inbar A, Sheridan G J and Lane P N J 2022 Performance of GEDI Space-Borne LiDAR for Quantifying Structural Variation in the Temperate Forests of South-Eastern Australia *Remote Sensing* **14** 3615

Dinerstein E, Olson D, Joshi A, Vynne C, Burgess N D, Wikramanayake E, Hahn N, Palminteri S, Hedao P, Noss R, Hansen M, Locke H, Ellis E C, Jones B, Barber C V, Hayes R, Kormos C, Martin V, Crist E, Sechrest W, Price L, Baillie J E M, Weeden D, Suckling K, Davis C, Sizer N, Moore R, Thau D, Birch T, Potapov P, Turubanova S, Tyukavina A, de Souza N, Pintea L, Brito J C, Llewellyn O A, Miller A G, Patzelt A, Ghazanfar S A, Timberlake J, Klöser H, Shennan-Farpón Y, Kindt R, Lillesø J-P B, van Breugel P, Graudal L, Voge M, Al-Shammari K F and Saleem M 2017 An Ecoregion-Based Approach to Protecting Half the Terrestrial Realm *Bioscience* **67** 534–45

Doyle E L, Graham H A, Boulton C A, Lenton T M, Feldpausch T R and Cunliffe A M 2025 Evaluating GEDI for quantifying forest structure across a gradient of degradation in Amazonian rainforests *Environ. Res. Lett.* **20** 054016

Dubayah R, Armston J, Healey S P, Bruening J M, Patterson P L, Kellner J R, Duncanson L, Saarela S, Ståhl G, Yang Z, Tang H, Blair J B, Fatoyinbo L, Goetz S, Hancock S, Hansen M, Hofton M, Hurtt G and Luthcke S 2022 GEDI launches a new era of biomass inference from space *Environ. Res. Lett.* **17** 095001

Dubayah R, Blair J B, Goetz S, Fatoyinbo L, Hansen M, Healey S, Hofton M, Hurtt G, Kellner J, Luthcke S, Armston J, Tang H, Duncanson L, Hancock S, Jantz P, Marselis S, Patterson P L, Qi W and Silva C 2020 The Global Ecosystem Dynamics Investigation: High-resolution laser ranging of the Earth's

forests and topography *Science of Remote Sensing* **1** 100002

Dubayah R, Hofton M, Blair J, Armston J, Tang H and Luthcke S 2021a GEDI L2A elevation and height metrics data global footprint level V002 Online: http://dx.doi.org/10.5067/GEDI/GEDI02_A.002

Dubayah R, Tang H, Armston J, Luthcke S, Hofton M and Blair J 2021b GEDI L2B canopy cover and vertical profile metrics data global footprint level V002 Online: http://dx.doi.org/10.5067/GEDI/GEDI02_B.002

Duncanson L, Kellner J R, Armston J, Dubayah R, Minor D M, Hancock S, Healey S P, Patterson P L, Saarela S, Marselis S, Silva C E, Bruening J, Goetz S J, Tang H, Hofton M, Blair B, Luthcke S, Fatoyinbo L, Abernethy K, Alonso A, Andersen H-E, Aplin P, Baker T R, Barbier N, Bastin J F, Biber P, Boeckx P, Bogaert J, Boschetti L, Boucher P B, Boyd D S, Burslem D F R P, Calvo-Rodriguez S, Chave J, Chazdon R L, Clark D B, Clark D A, Cohen W B, Coomes D A, Corona P, Cushman K C, Cutler M E J, Dalling J W, Dalponte M, Dash J, de-Miguel S, Deng S, Ellis P W, Erasmus B, Fekety P A, Fernandez-Landa A, Ferraz A, Fischer R, Fisher A G, García-Abril A, Gobakken T, Hacker J M, Heurich M, Hill R A, Hopkinson C, Huang H, Hubbell S P, Hudak A T, Huth A, Imbach B, Jeffery K J, Katoh M, Kearsley E, Kenfack D, Kljun N, Knapp N, Král K, Krůček M, Labrière N, Lewis S L, Longo M, Lucas R M, Main R, Manzanera J A, Martínez R V, Mathieu R, Memiaghe H, Meyer V, Mendoza A M, Monerris A, Montesano P, Morsdorf F, Næsset E, Naidoo L, Nilus R, O'Brien M, Orwig D A, Papathanassiou K, Parker G, Philipson C, Phillips O L, Pisek J, Poulsen J R, et al 2022 Aboveground biomass density models for NASA's Global Ecosystem Dynamics Investigation (GEDI) lidar mission *Remote Sens. Environ.* **270** 112845

Duncanson L, Neuenschwander A, Hancock S, Thomas N, Fatoyinbo T, Simard M, Silva C A, Armston J, Luthcke S B, Hofton M, Kellner J R and Dubayah R 2020 Biomass estimation from simulated GEDI, ICESat-2 and NISAR across environmental gradients in Sonoma County, California *Remote Sens. Environ.* **242** 111779

Ehbrecht M, Seidel D, Annighöfer P, Kreft H, Köhler M, Zemp D C, Puettmann K, Nilus R, Babweteera F, Willim K, Stiers M, Soto D, Boehmer H J, Fisichelli N, Burnett M, Juday G, Stephens S L and Ammer C 2021 Global patterns and climatic controls of forest structural complexity *Nat. Commun.* **12** 519

Favrichon S, Lee J, Yang Y, Dalagnol R, Wagner F, Sagang L B and Saatchi S 2025 Monitoring changes of forest height in California *Front. Remote Sens.* **5** Online: https://www.frontiersin.org/journals/remote-sensing/articles/10.3389/frsen.2024.1459524/epub

Fink D, Hochachka W M, Zuckerberg B, Winkler D W, Shaby B, Munson M A, Hooker G, Riedewald M, Sheldon D and Kelling S 2010 Spatiotemporal exploratory models for broad-scale survey data *Ecol. Appl.* **20** 2131–47

Finley A O 2011 Comparing spatially-varying coefficients models for analysis of ecological data with non-stationary and anisotropic residual dependence: Spatially-varying coefficients models *Methods Ecol. Evol.* **2** 143–54

Gao B-C 1996 NDWI—A normalized difference water index for remote sensing of vegetation liquid water from space *Remote Sens. Environ.* **58** 257–66

Gorelick N, Hancher M, Dixon M, Ilyushchenko S, Thau D and Moore R 2017 Google Earth Engine: Planetary-scale geospatial analysis for everyone *Remote Sens. Environ.* **202** 18–27

Gough C M, Atkins J W, Fahey R T and Hardiman B S 2019 High rates of primary production in structurally complex forests *Ecology* **100** e02864

Hakkenberg C R and Goetz S J 2021 Climate mediates the relationship between plant biodiversity and forest structure across the United States *Glob. Ecol. Biogeogr.* **30** 2245–58

Hancock S, Armston J, Hofton M, Sun X, Tang H, Duncanson L I, Kellner J R and Dubayah R 2019 The GEDI simulator: A large-footprint waveform lidar simulator for calibration and validation of spaceborne missions *Earth Space Sci.* **6** 294–310

He C, Shi P, Xie D and Zhao Y 2010 Improving the normalized difference built-up index to map urban built-up areas using a semiautomatic segmentation approach *Remote Sens. Lett.* **1** 213–21

Hofton M and Blair J B 2019 Algorithm Theoretical Basis Document (ATBD) for GEDI Transmit and Receive Waveform Processing for L1 and L2 Products *NASA EOSDIS Land Processes Distributed Active Archive Center* Online: https://lpdaac.usgs.gov/documents/581/GEDI_WF_ATBD_v1.0.pdf

Huete A, Didan K, Miura T, Rodriguez E P, Gao X and Ferreira L G 2002 Overview of the radiometric and biophysical performance of the MODIS vegetation indices *Remote Sens. Environ.* **83** 195–213

Hu X, Li L, Huang J, Zeng Y, Zhang S, Su Y, Hong Y and Hong Z 2024 Radar vegetation indices for monitoring surface vegetation: Developments, challenges, and trends *Sci. Total Environ.* **945** 173974

Kacic P, Hirner A and Da Ponte E 2021 Fusing Sentinel-1 and -2 to Model GEDI-Derived Vegetation Structure Characteristics in GEE for the Paraguayan Chaco *Remote Sensing* **13** 5105

Kacic P, Thonfeld F, Gessner U and Kuenzer C 2023 Forest structure characterization in Germany: Novel products and analysis based on GEDI, Sentinel-1 and Sentinel-2 data *Remote Sens. (Basel)* **15** 1969

Karra K, Kontgis C, Statman-Weil Z, Mazzariello J C, Mathis M and Brumby S P 2021 Global land use / land cover with Sentinel 2 and deep learning *2021 IEEE International Geoscience and Remote Sensing Symposium IGARSS* IGARSS 2021 - 2021 IEEE International Geoscience and Remote Sensing Symposium (IEEE) Online: https://www.semanticscholar.org/paper/Global-land-use-land-cover-with-Sentinel-2-and-deep-Karra-Kontgis/76caafae9c08411d6727c816cbdb987ef3e1d0f1

Key C H and Benson N C 2006 Landscape Assessment (LA) *FIREMON: Fire effects monitoring and inventory system* (Fort Collins, CO: U.S. Department of Agriculture, Forest Service, Rocky Mountain Research Station) pp LA – 1–55

Killion A K, Honda A, Trout E and Carter N H 2023 Integrating spaceborne estimates of structural diversity of habitat into wildlife occupancy models *Environ. Res. Lett.* **18** 065002

Kim Y and van Zyl J J 2009 A time-series approach to estimate soil moisture using polarimetric radar data *IEEE Trans. Geosci. Remote Sens.* **47** 2519–27

Kim Y and van Zyl J 2004 Vegetation effects on soil moisture estimation *IEEE International IEEE International IEEE International Geoscience and Remote Sensing Symposium, 2004. IGARSS '04. Proceedings. 2004* IEEE International IEEE International IEEE International Geoscience and Remote Sensing Symposium, 2004. IGARSS '04. Proceedings. 2004 vol 2 (IEEE) pp 800–2

Lahssini K, Baghdadi N, le Maire G and Fayad I 2022 Influence of GEDI Acquisition and Processing Parameters on Canopy Height Estimates over Tropical Forests *Remote Sensing* **14** 6264

Lang N, Jetz W, Schindler K and Wegner J D 2023 A high-resolution canopy height model of the Earth *Nat Ecol Evol* **7** 1778–89

LaRue E A, Fahey R T, Alveshere B C, Atkins J W, Bhatt P, Buma B, Chen A, Cousins S, Elliott J M, Elmore A J, Hakkenberg C R, Hardiman B S, Johnson J S, Kashian D M, Koirala A, Papeş M, St Hilaire J B, Surasinghe T D, Zambrano J, Zhai L and Fei S 2023 A theoretical framework for the ecological role of three‐dimensional structural diversity *Front. Ecol. Environ.* **21** 4–13

Liu L, Zhang X and Zhao T 2023 GLC_FCS30D: the first global 30-m land-cover dynamic monitoring product with fine classification system from 1985 to 2022 *GLC_FCS30D: the first global 30 m land-cover dynamics monitoring product with a fine classification system for the period from 1985 to 2022 generated using dense-time-series Landsat imagery and the continuous change-detection method* Online: https://zenodo.org/records/8239305

Liu X, Moudrý V, Schuldt B and Forkel M 2025 GEDI reveals decline in overstorey and increase in understorey canopy cover of protected forests in Central Europe since 2019 *For. Ecol. Manage.* **597** 123155

Li W, Guo W-Y, Pasgaard M, Niu Z, Wang L, Chen F, Qin Y and Svenning J-C 2023 Human fingerprint on structural density of forests globally *Nat. Sustain.* **6** 368–79

Li X, Li L, Ni W, Mu X, Wu X, Vaglio Laurin G, Vangi E, Stereńczak K, Chirici G, Yu S and Huang H 2024a Validating GEDI tree canopy cover product across forest types using co-registered aerial LiDAR data *ISPRS J. Photogramm. Remote Sens.* **207** 326–37

Li X, Wessels K, Armston J, Duncanson L, Urbazaev M, Naidoo L, Mathieu R and Main R 2024b Evaluation of GEDI footprint level biomass models in Southern African Savannas using airborne LiDAR and field measurements *Science of Remote Sensing* **10** 100161

Loiseau T, Arrouays D, Richer-de-Forges A C, Lagacherie P, Ducommun C and Minasny B 2021 Density of soil observations in digital soil mapping: A study in the Mayenne region, France *Geoderma Reg.* **24** e00358

Lu G Y and Wong D W 2008 An adaptive inverse-distance weighting spatial interpolation technique *Comput. Geosci.* **34** 1044–55

MacArthur R H and MacArthur J W 1961 On bird species diversity *Ecology* **42** 594–8

Marselis S M, Keil P, Chase J M and Dubayah R 2022 The use of GEDI canopy structure for explaining variation in tree species richness in natural forests *Environ. Res. Lett.* **17** 045003

Masek J, Ju J, Roger J, Skakun S, Vermote E, Claverie M, Dungan J, Yin Z, Freitag B and Justice C 2021 HLS Operational Land Imager Surface Reflectance and TOA Brightness Daily Global 30m v2.0 Online: https://lpdaac.usgs.gov/products/hlsl30v002/

Mastro P, Peppo M D, Crema A, Boschetti M and Pepe A 2023 Statistical characterization and exploitation of Synthetic Aperture radar vegetation indexes for the generation of Leaf area Index time series *Int. J. Appl. Earth Obs. Geoinf.* **124** 103498

Mohammadpour P, Viegas D X, Pereira A and Chuvieco E 2025 Multitemporal Sentinel and GEDI data integration for overstory and understory fuel type classification *Int. J. Appl. Earth Obs. Geoinf.* **139** 104455

Moreno-Martínez Á, Camps-Valls G, Kattge J, Robinson N, Reichstein M, van Bodegom P, Kramer K, Cornelissen J H C, Reich P, Bahn M, Niinemets Ü, Peñuelas J, Craine J M, Cerabolini B E L, Minden V, Laughlin D C, Sack L, Allred B, Baraloto C, Byun C, Soudzilovskaia N A and Running S W 2018 A methodology to derive global maps of leaf traits using remote sensing and climate data *Remote Sens. Environ.* **218** 69–88

Nadkarni N M, McIntosh A C S and Cushing J B 2008 A framework to categorize forest structure concepts *For. Ecol. Manage.* **256** 872–82

Nasiri V, Hawryło P, Tompalski P, Wertz B and Socha J 2025 Linking remotely sensed growth-related canopy attributes to interannual tree-ring width variations: A species-specific study using Sentinel optical and SAR time series *ISPRS J. Photogramm. Remote Sens.* **221** 347–62

Nasirzadehdizaji R, Balik Sanli F, Abdikan S, Cakir Z, Sekertekin A and Ustuner M 2019 Sensitivity analysis of multi-temporal Sentinel-1 SAR parameters to crop height and canopy coverage *Appl. Sci. (Basel)* **9** 655

Ngo Y-N, Ho Tong Minh D, Baghdadi N and Fayad I 2023 Tropical forest top height by GEDI: From sparse coverage to continuous data *Remote Sens. (Basel)* **15** 975

Pasquarella V J, Brown C F, Czerwinski W and Rucklidge W J 2023 Comprehensive quality assessment of optical satellite imagery using weakly supervised video learning *2023 IEEE/CVF Conference on Computer Vision and Pattern Recognition Workshops (CVPRW)* 2023 IEEE/CVF Conference on Computer Vision and Pattern Recognition Workshops (CVPRW) (IEEE) pp 2125–35

Poggio L, de Sousa L M, Batjes N H, Heuvelink G B M, Kempen B, Ribeiro E and Rossiter D 2021 SoilGrids 2.0: producing soil information for the globe with quantified spatial uncertainty *SOIL* **7** 217–40

Potapov P, Li X, Hernandez-Serna A, Tyukavina A, Hansen M C, Kommareddy A, Pickens A, Turubanova S, Tang H, Silva C E, Armston J, Dubayah R, Blair J B and Hofton M 2021 Mapping global forest canopy height through integration of GEDI and Landsat data *Remote Sens. Environ.* **253** 112165

Qiu S, Zhu Z and He B 2019 Fmask 4.0: Improved cloud and cloud shadow detection in Landsats 4–8 and Sentinel-2 imagery *Remote Sens. Environ.* **231** 111205

Quegan S, Le Toan T, Chave J, Dall J, Exbrayat J-F, Minh D H T, Lomas M, D'Alessandro M M, Paillou P, Papathanassiou K, Rocca F, Saatchi S, Scipal K, Shugart H, Smallman T L, Soja M J, Tebaldini S, Ulander L, Villard L and Williams M 2019 The European Space Agency BIOMASS mission: Measuring forest above-ground biomass from space *Remote Sens. Environ.* **227** 44–60

Ray T, Delory B M, Beugnon R, Bruelheide H, Cesarz S, Eisenhauer N, Ferlian O, Quosh J, von Oheimb G and Fichtner A 2023 Tree diversity increases productivity through enhancing structural complexity across mycorrhizal types *Sci. Adv.* **9** eadi2362

Ren C, Jiang H, Xi Y, Liu P and Li H 2023 Quantifying temperate forest diversity by integrating GEDI LiDAR and multi-temporal Sentinel-2 imagery *Remote Sens. (Basel)* **15** 375

Rex F E, Silva C A, Broadbent E N, Dalla Corte A P, Leite R, Hudak A, Hamamura C, Latifi H, Xiao J, Atkins J W, Amaral C, Cunha Neto E M da, Cardil A, Almeyda Zambrano A M, Liesenberg V, Liang J, De Almeida D R A and Klauberg C 2025 Spatial characterization of woody species diversity in tropical savannas using GEDI and optical data *Sensors (Basel)* **25** 308

Rikimaru A, Roy P S, Miyatake S and Others 2002 Tropical forest cover density mapping *Trop. Ecol.* **43** 39–47

Rishmawi K, Huang C, Schleeweis K and Zhan X 2022 Integration of VIIRS observations with GEDI-LiDAR measurements to monitor forest structure dynamics from 2013 to 2020 across the conterminous United States *Remote Sens. (Basel)* **14** 2320

Rishmawi K, Huang C and Zhan X 2021 Monitoring Key Forest Structure Attributes across the Conterminous United States by Integrating GEDI LiDAR Measurements and VIIRS Data *Remote Sensing* **13** 442

Rouse J W Jr, Haas R H, Schell J A and Deering D W 1974 Monitoring Vegetation Systems in the Great Plains with Erts *NASA Special Publication* vol 351 p 309

Schlickmann M B, Bueno I T, Valle D, Hammond W M, Prichard S J, Hudak A T, Klauberg C, Karasinski M A, Brock K M, Rocha K D, Xia J, Vieira Leite R, Higuchi P, da Silva A C, Maximo da Silva G, Cova G R and Silva C A 2025 Statewide forest canopy cover mapping of Florida using synergistic integration of spaceborne LiDAR, SAR, and optical imagery *Remote Sens. (Basel)* **17** 320

Schlund M and Erasmi S 2020 Sentinel-1 time series data for monitoring the phenology of winter wheat *Remote Sens. Environ.* **246** 111814

Seyrek E C, Narin O G and Uysal M 2025 Forest canopy cover estimation with machine learning using GEDI and Landsat data in the Western Marmara Region, Türkiye *Earth Sci. Inform.* **18** 1–18

Sherman R, Mullen R, Haomin L, Zhendong F and Yi W 2008 Spatial patterns of plant diversity and communities in Alpine ecosystems of the Hengduan Mountains, northwest Yunnan, China *Journal of Plant Ecology* **1** 117–36

Shi T and Xu H 2019 Derivation of Tasseled Cap Transformation Coefficients for Sentinel-2 MSI At-Sensor Reflectance Data *IEEE Journal of Selected Topics in Applied Earth Observations and Remote Sensing* **12** 4038–48

Sothe C, Gonsamo A, Lourenço R B, Kurz W A and Snider J 2022 Spatially continuous mapping of forest canopy height in Canada by combining GEDI and ICESat-2 with PALSAR and Sentinel *Remote Sens. (Basel)* **14** 5158

Stein A, Gerstner K and Kreft H 2014 Environmental heterogeneity as a universal driver of species richness across taxa, biomes and spatial scales *Ecol. Lett.* **17** 866–80

Tadono T, Nagai H, Ishida H, Oda F, Naito S, Minakawa K and Iwamoto H 2016 Generation of the 30 M-Mesh Global Digital Surface Model by Alos Prism *ISPRS - International Archives of the Photogrammetry, Remote Sensing and Spatial Information Sciences* **41B4** 157

Takaku J, Tadono T, Doutsu M, Ohgushi F and Kai H 2020 Updates of "aw3d30" Alos global digital surface model with other open access datasets *ISPRS - Int. Arch. Photogramm. Remote Sens. Spat. Inf. Sci.* **XLIII-B4-2020** 183–9

Takaku J, Tadono T, Tsutsui K and Ichikawa M 2016 VALIDATION OF'AW3D'GLOBAL DSM GENERATED FROM ALOS PRISM *ISPRS Annals of Photogrammetry, Remote Sensing & Spatial Information Sciences* **3** Online: http://www.aw3d.jp/wp/wp-content/themes/AW3DJapanese/technology/doc/pdf/technology_01.pdf

Tamiminia H, Salehi B, Mahdianpari M and Goulden T 2024 State-wide forest canopy height and aboveground biomass map for New York with 10 m resolution, integrating GEDI, Sentinel-1, and Sentinel-2 data *Ecol. Inform.* **79** 102404

Tang H, Stoker J, Luthcke S, Armston J, Lee K, Blair B and Hofton M 2023 Evaluating and mitigating the impact of systematic geolocation error on canopy height measurement performance of GEDI *Remote Sens. Environ.* **291** 113571

Theobald D M, Harrison-Atlas D, Monahan W B and Albano C M 2015 Ecologically-Relevant Maps of Landforms and Physiographic Diversity for Climate Adaptation Planning *PLoS One* **10** e0143619

Tucker C J 1979 Red and photographic infrared linear combinations for monitoring vegetation *Remote Sens. Environ.* **8** 127–50

Uuemaa E, Ahi S, Montibeller B, Muru M and Kmoch A 2020 Vertical Accuracy of Freely Available Global Digital Elevation Models (ASTER, AW3D30, MERIT, TanDEM-X, SRTM, and NASADEM) *Remote Sensing* **12** 3482

Vogeler J C, Fekety P A, Elliott L, Swayze N C, Filippelli S K, Barry B, Holbrook J D and Vierling K T 2023 Evaluating GEDI data fusions for continuous characterizations of forest wildlife habitat *Frontiers in Remote Sensing* **4** Online: https://www.frontiersin.org/articles/10.3389/frsen.2023.1196554

Wei C, Sweeney C, Roberts T, Fink D, Zuckerberg B, Jarzyna M A and Zhao K 2024 Characterizing temperate vegetation structure in eastern north America using GEDI (abstract ID: B33A-1535) *ESS Open Archive* Online: http://dx.doi.org/10.22541/essoar.173395729.91702478/v1

Wilson A M, Latimer A M and Silander J A Jr 2015 Climatic controls on ecosystem resilience: Postfire regeneration in the Cape Floristic Region of South Africa *Proc. Natl. Acad. Sci. U. S. A.* **112** 9058–63

Xu H 2006 Modification of normalised difference water index (NDWI) to enhance open water features in remotely sensed imagery *Int. J. Remote Sens.* **27** 3025–33

Xu J, Coleman K, Radeloff V C, Songer M and Huang Q 2025 Modeling worldwide tree biodiversity using canopy structure metrics from Global Ecosystem Dynamics Investigation data *Remote Sens. (Basel)* **17** 1408

Xu J, Farwell L, Radeloff V C, Luther D, Songer M, Cooper W J and Huang Q 2024 Avian diversity across guilds in North America versus vegetation structure as measured by the Global Ecosystem Dynamics Investigation (GEDI) *Remote Sens. Environ.* **315** 114446

Zellweger F, De Frenne P, Lenoir J, Vangansbeke P, Verheyen K, Bernhardt-Römermann M, Baeten L, Hédl R, Berki I, Brunet J, Van Calster H, Chudomelová M, Decocq G, Dirnböck T, Durak T, Heinken T, Jaroszewicz B, Kopecký M, Máliš F, Macek M, Malicki M, Naaf T, Nagel T A, Ortmann-Ajkai A, Petřík P, Pielech R, Reczyńska K, Schmidt W, Standovár T, Świerkosz K, Teleki B, Vild O, Wulf M and Coomes D 2020 Forest microclimate dynamics drive plant responses to warming *Science* **368** 772–5

Zhai Y, Roy D P, Martins V S, Zhang H K, Yan L and Li Z 2022 Conterminous United States Landsat-8 top of atmosphere and surface reflectance tasseled cap transformation coefficients *Remote Sens. Environ.* **274** 112992

Zhang W, Xi Y, Brandt M, Ren C, Bai J, Ma Q and Fensholt R 2024a Stand structure of tropical forests is strongly associated with primary productivity *Commun. Earth Environ.* **5** 1–9

Zhang X, Zhao T, Xu H, Liu W, Wang J, Chen X and Liu L 2024b GLC_FCS30D: the first global 30 m land-cover dynamics monitoring product with a fine classification system for the period from 1985 to 2022 generated using dense-time-series Landsat imagery and the continuous change-detection method *Earth System Science Data* **16** 1353–81

Zhu Z, Wang S and Woodcock C E 2015 Improvement and expansion of the Fmask algorithm: cloud, cloud shadow, and snow detection for Landsats 4–7, 8, and Sentinel 2 images *Remote Sens. Environ.* **159** 269–77

Ziegler A, Heisig J, Ludwig M, Reudenbach C, Meyer H and Nauss T 2023 Using GEDI as training data for an ongoing mapping of landscape-scale dynamics of the plant area index *Environ. Res. Lett.* **18** 075003